Environ Fluid Mech (2014) 14:1303–1334
DOI 10.1007/s10652-014-9336-5

ORIGINAL ARTICLE

The role of rooted emergent vegetation on periodically thermal-driven flow over a sloping bottom

Ying-Tien Lin · Chin H. Wu

Received: 6 July 2013 / Accepted: 7 January 2014 / Published online: 2 February 2014

Abstract Thermal-driven flow is generated due to topographic or vegetation-shading effects. Asymptotic solutions by assuming a small bottom slope are derived to discuss effects of rooted emergent vegetation and interactions between emergent vegetation and sloping topography on thermal-driven flow during diurnal heating and cooling cycles. The results show that the zero-order horizontal velocity is significantly reduced by vegetative drag, and the time lag between the change of horizontal velocity and the reversal of pressure gradient is also shortened. The solutions reveal that the viscous effect is dominant in very shallow water, and the drag force becomes important as the water depth increases. The inertial term is only important at the very beginning stage of flow initiation. Different vegetation distributions can significantly change the temperature fields that then affect patterns of thermal-driven circulation and exchange flowrates. For the case of tall vegetation growth in shallow water, and when the deep water side is open, the effects of vegetation shading may interfere with the topographic effects and dramatically alter the flow patterns. The blockage of solar radiation due to vegetation shading can determine the patterns and magnitude of thermal-driven flow. By means of the derived asymptotic horizontal velocity, exchange flow rates can be estimated, which are in good agreement with previous studies. The limitation and valid ranges of asymptotic solutions are finally discussed.

Keywords Thermal-driven flow · Sloping bottom · Rooted emergent vegetation · Diurnal heating and cooling

Y.-T. Lin (✉)
Disaster Prevention and Water Environment Research Center, National Chiao Tung University, Hisnchu 300, Taiwan
e-mail: kevinlin@ntu.edu.tw

C. H. Wu
Department of Civil and Environmental Engineering, University of Wisconsin-Madison, Madison, WI 53706, USA

1 Introduction

Thermal-driven flow, also called the natural convection flow, in the absence of wind forcing, arises from heterogeneous temperature distribution and subsequent variations of density gradients in fluids [1,2]. For example, horizontal transport of thermal-driven flows due to differential surface heating or cooling is commonly observed in the effects of vegetation shading [3] or sloping bathymetry [4] of lakes or geophysical fluid bodies. Existence of emergent vegetation can block some solar radiation into the water body, yielding temperature in the vegetation-shading area to be cooler than that in open water or less vegetated areas during daytime [5–7]. During nighttime, emergent vegetation reduces radiation losses from water surface, producing higher temperature in the vegetation region [8]. The differential heating due to vegetation shading thereby results in the variation of water densities, driving thermal-driven circulation from the open water to the vegetated area along the surface, returning to the open water along the bottom during daytime, and reversing the circulation patterns during nighttime. Similarly, on a sloping topographic bottom during daytime, the same amount of solar radiation that enters into the water body leads to warmer water in the shallow region in comparison with the deeper region. As a result, the induced circulation, which flows from the shallow water to the deep water along the water surface and underflow uphill over the sloping bottom toward the nearshore, is generated. During night-time the induced circulation is then reverse. The diurnal heating and cooling can generate the thermal-driven circulation to move back and forth, enhancing the exchange of nutrient and chemical substances and reducing the flushing time between the nearshore and the main water bodies [2]. The magnitude for such thermal-driven circulation can reach up to 10–15 cm/s, much faster than turbulence diffusion alone [1,9]. The horizontal thermal-driven flow, "thermal siphon," pumping water in and out in littoral zones, is an important mechanism for the renewal of the littoral water [1].

Previously, several studies have examined the horizontal thermal-driven flow over a sloping bottom. Observations conducted by Adam and Wells [10] and Monismith et al. [1] showed a significant time lag (or spin-up time), up to 12 h, of the circulation in response to the changes of diurnal heating and cooling forcing in littoral regions of natural lakes. To investigate the relationship between the time lag and dominant physical processes, Farrow and Patterson [4] (from here on referred to as FP93) derived a zero-order asymptotic solution by neglecting nonlinear convective effects for a small slope triangular cavity model under the assumption of uniformly distributed heat over the water column. It was found that in shallow water, the time taken for viscosity response over the whole water depth is relatively short. The horizontal velocity immediately responds to the changes in the horizontal pressure gradient due to diurnal forcing. In deep water, the inertia of fluid balances with the horizontal pressure, and the horizontal velocity exhibits a phase lag of a quarter period of the forcing. Moreover, the vertical velocity profile is characterized by this balance until viscosity diffuses into the whole water column. Recognizing that the zero-order asymptotic solution is not valid near the tip of the wedge where nonlinearity becomes important, Farrow [11] (hereafter referred to as F04) extended the work of FP93 to the second-order temperature solution to include the effects of heat conduction and nonlinear advection. Asymptotic solutions and numerical simulations both showed that the horizontal advective heat transfer generated from the second-order temperature profile shows a viscous-dominated mechanism in shallow water and an inertia-dominated flow in deep water [11]. To simulate more realistic heating processes, Farrow and Patterson [12], Lai and Patterson [13], and Mao et al. [14] employed an exponential decay function for solar radiation over the water depth, different from the previous assumption of a uniform heating distribution. Their results showed that heat-transfer processes are related

to dimensionless Rayleigh number and can be classified as three (e.g., conduction, transient, and convection) dominant regimes to trigger flow over a small bottom slope. Lei and Patterson [15] revealed that thermal instability is crucial in deep water to break residual flow and reverse the circulation during diurnal cycles. Recently Mao et al. [14,16] further showed that flow properties and stability of the thermal boundary layer are related to the horizontal location in the wedge domain both during the heating and cooling periods. Farrow [17] discussed the wind effects on thermal-driven flow near the shore of a lake. Overall, previous studies have gained a very good understanding on thermal-driven flow during diurnal cycles.

Shading effects from floating or emergent vegetation, commonly seen in aquatic system, can also induce horizontal temperature differences which then generate the convective circulation [5,7]. Previous studies [5,18] on the thermal-driven flow from the shading of floating vegetation over a flat bottom have identified both inertial and energy-limited regions, depending on the corresponding magnitudes of the circulation. Oldham and Sturman [19], and Zhang and Nepf [9,20] showed that rooted emergent vegetation, unlike floating vegetation, provides inherent drag to slow down the generated circulation. Furthermore, both horizontal velocity and volumetric flowrate of exchange flow can be strongly reduced with the increasing vegetation densities [20,21]. Oldham and Sturm [19] applied porous media flow theory to study the impact of vegetative drag on exchange flow over a surface cooling cycle. Vegetative drag significantly reduces exchange flowrate and increases flushing time over vegetated regions. Zhang and Nepf [9] observed at the initial stage the exchange flow is inertia-dominated and quickly converted to be drag-dominated. The thickness of an intrusion layer corresponds to the length scale of light penetration. Recently Zhang and Nepf [22] showed that floating root vegetation can block the flow as flow intrusion length increases, and the exchange flow occurs only beneath the root layer. These works have provided new insight to reveal the role of vegetation on the thermal-driven flow. Nevertheless the effects of vegetative drag on the time-lag and dominant mechanisms including viscosity, inertia, and horizontal pressure gradient of the thermal-driven flow have not been well-identified. Also littoral vegetation is commonly observed over a slope, instead of ideal flat bottom. Furthermore, in shallow water, emergent vegetation is usually found because of abundant light and nutrients and blocks some solar radiation into the water body. Under this situation, shading from emergent vegetation causes cooler water temperature during daytime, a contradictory trend as warmer in shallow water found over an unvegetated sloping bottom. Consequently water temperature in shallow water thereby may not be always warmer than that in deep water. While previous studies have examined thermal-driven flow due to vegetation shading mainly over a flat bottom [5,7,9], the competition or interplay between vegetation shading and topographic sloping bottom on horizontal temperature gradient as well as thermal-driven flow has not yet been unveiled.

In this paper, an analytic approach is employed to examine thermal-driven flow generated by vegetation-shading and topographic effects during diurnal cycles. Asymptotic solutions including zero-order horizontal velocity and second-order temperature for thermal-driven flow within rooted emergent vegetation are derived. Based on the analytic velocity and temperature profiles, the spatial and temporal dominant mechanisms to balance between viscosity, vegetative drag, inertia and buoyancy are revealed and compared with experimental findings from Zhang and Nepf [9]. The asymptotic solutions are then used to examine the flow patterns in different vegetation distributions over a sloping bottom in terms of the competition between vegetation-shading and topographic effects. In addition, the derived zero-order horizontal velocity is used to estimate exchange flow rates at different water depths. The validity and feasibility of the asymptotic solutions are finally discussed.

2 Mathematical formulation

2.1 Governing equations, initial and boundary conditions

The thermal-driven flow with rooted emergent vegetation over a sloping boundary is schematized in Fig. 1. The wedge shape domain (x', z') is considered as a two-dimensional flow with the origin at the tip; $x'$and z' $(= -Sx')$ are the horizontal and vertical coordinates, respectively, where S is the bottom slope. For simplicity, the effect of vegetation leaf is neglected, i.e., the cross sectional area of the stem is constant vertically. The distribution of rooted emergent vegetation can vary along the x' direction but is assumed to be vertically uniform. The drag due to vegetation is assumed to be only applied in the horizontal direction and described as a quadratic drag law, which is $\frac{C_D a u'|u'|}{2}$, where u' is the horizontal velocity, C_D is the drag coefficient, and a is the frontal area of vegetation per unit volume [21]. The diurnal solar radiation is modeled as $I_0 \cos(2\pi t'/\tau)$ W m^{-2}, a periodic heat source, where I_0 is the bulk solar radiation intensity at the water surface, τ is the forcing period of 24 h, t' is time, and $t' = 0$ corresponds to noon. Here, we assumed the solar radiation is uniformly distributed over the local water depth, which is a considerable simplification to provide analytic processes (FP93, F04 [17]). The internal heat source uniformly distributed over the water depth is then described as

$$Q_{\text{heat}}(x', z', t') = \frac{I_0 M(x') \cos(2\pi t'/\tau)}{\rho_0 C_p S x'}, \tag{1}$$

where Sx' denotes the local water depth where the solar radiation is distributed, ρ_0 is the reference density of fluid, and C_p is the specific heat of water. In Eq. (1), $M(x')$ represents how distribution of emergent vegetation reduces solar radiation penetrating into the water column. We will discuss $M(x')$ more in detail later.

With the above assumptions and the Boussinesq approximation due to relatively small temperature differences in the aquatic system, the two-dimensional governing equations of flow motions are

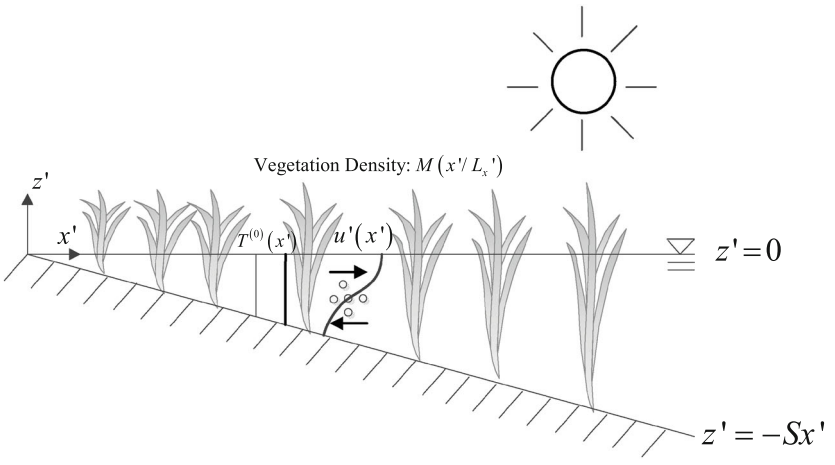

Fig. 1 Geometry of the domain showing the coordinate system and vegetation distribution. Distribution of emergent vegetation is only function of the horizontal location x'

$$n_{\mathrm{v}}\left(\frac{\partial u'}{\partial x'}+\frac{\partial w'}{\partial z'}\right)=0, \tag{2}$$

$$n_{\mathrm{v}}\left(\frac{\partial u'}{\partial t'}+u'\frac{\partial u'}{\partial x'}+w'\frac{\partial u'}{\partial z'}\right)=-\frac{n_{\mathrm{v}}}{\rho_0}\frac{\partial P'}{\partial x'}-\frac{C_{\mathrm{D}}au'\left|u'\right|}{2}+n_{\mathrm{v}}\nu\left(\frac{\partial^2 u'}{\partial x'^2}+\frac{\partial^2 u'}{\partial z'^2}\right), \tag{3}$$

$$n_{\mathrm{v}}\left(\frac{\partial w'}{\partial t'}+u'\frac{\partial w'}{\partial x'}+w'\frac{\partial w'}{\partial z'}\right)=-\frac{n_{\mathrm{v}}}{\rho_0}\frac{\partial P'}{\partial z'}+n_{\mathrm{v}}\nu\left(\frac{\partial^2 w'}{\partial x'^2}+\frac{\partial^2 w'}{\partial z'^2}\right)+n_{\mathrm{v}}g\alpha\left(T'-T_0\right), \tag{4}$$

$$n_{\mathrm{v}}\left(\frac{\partial T'}{\partial t'}+u'\frac{\partial T'}{\partial x'}+w'\frac{\partial T'}{\partial z'}\right)=n_{\mathrm{v}}\left[\kappa\left(\frac{\partial^2 T'}{\partial x'^2}+\frac{\partial^2 T'}{\partial z'^2}\right)+Q_{\mathrm{heat}}\left(x',z',t'\right)\right], \tag{5}$$

where u', w' are the horizontal and vertical velocity, P' is the pressure, ν is the kinematic viscosity of water, g is the gravity acceleration, α is the thermal expansion coefficient, $T'$is the temperature, T_0 is the reference temperature, and n_{v} is the porosity, which is the volume fraction occupied by water within vegetation [21].

Under low stem Reynolds number $\mathrm{Re_d}$ ($=u'd/\nu$, where d is the stem diameter of vegetation), C_{D} is inversely proportional to $\left|u'\right|$, i.e., $C_{\mathrm{D}}=\frac{2n_{\mathrm{v}}C}{|u'|}$, where C is a linear drag coefficient [20]. Equation (3) can be thus simplified as:

$$\frac{\partial u'}{\partial t'}+u'\frac{\partial u'}{\partial x'}+w'\frac{\partial u'}{\partial z'}=-\frac{1}{\rho_0}\frac{\partial P'}{\partial x'}-Cau'+\nu\left(\frac{\partial^2 u'}{\partial x'^2}+\frac{\partial^2 u'}{\partial z'^2}\right). \tag{6}$$

According to numerical results of Koch and Ladd [23], a regression relationship between the linear drag coefficient C and the solid volume fraction ϕ ($=1-n_{\mathrm{v}}$) can be obtained: $C=-0.3788\phi^2+0.1134\phi$. The frontal area a for circular-stemmed vegetation is equal to $\frac{4\phi}{\pi d}$, where d is the diameter of vegetation stem.

Initially, fluids are at rest and isothermal. Since the entire heat input/output is included in the internal heat source Q_{heat}, there are no fluxes across any of the boundaries, that is, the thermal boundary conditions are insulated over the surface and bottom (FP93). At the surface, it is shear free due to the absence of wind or other momentum forcing, and no flow occurs across the surface. For the bottom, the flow is impermeable to the bottom, and abides by the no-slip condition. In summary, the initial and boundary conditions are:

$$\begin{aligned}
&T'=T_0, \quad u'=w'=0 \quad \text{at } t=0,\\
&\frac{\partial T'}{\partial z'}=0, \quad \frac{\partial u'}{\partial z'}=0 \text{ (shear free)}, \quad w'=0 \quad \text{on } z'=0,\\
&\frac{\partial T'}{\partial \widehat{n}}=0, \quad u'=w'=0 \text{ (no slip)} \quad \text{on } z'=-Sx',
\end{aligned} \tag{7}$$

where $\widehat{n}$ is the direction normal to the sloping bottom.

2.2 Scaling analysis

The governing equations are nondimensionalized as follows. The dominant time scale is characterized by the period of forcing τ, i.e., 24 h. The vertical length scale H is defined as the growth of the boundary layer during one diurnal cycle, i.e., $H=\sqrt{\nu\tau}$ (FP93). Due to the geometry of the wedge, the horizontal length scale L is obtained by combining the slope S and vertical scale H, i.e., $x'\sim L=H/S$. Balancing the unsteady and heat source terms in Eq. (4) gives the temperature scale $T'-T_0=\Delta T\sim\frac{I_0\tau}{\rho_0 C_{\mathrm{p}}\sqrt{\nu\tau}}$. The balancing of the temperature difference with hydrostatic pressure yields a pressure scale $P'\sim\frac{g\alpha I_0\tau}{c_{\mathrm{p}}}$. By

substituting the pressure scale into Eq. (3) and assuming the pressure force is balanced by the unsteady horizontal velocity, the scale of horizontal velocity is $u' \sim SGr\sqrt{\nu/\tau}$, where the Grashof number is $\mathrm{Gr} = \frac{g\alpha I_0 \tau^2}{\rho_0 C_p \nu}$. By use of the continuity equation, the scale for the vertical velocity is $w' \sim S^2\mathrm{Gr}\sqrt{\nu/\tau}$.

Using the scales described above, the non-dimensional energy equation becomes

$$\frac{\partial T}{\partial t} + S^2\mathrm{Gr}\left(u\frac{\partial T}{\partial x} + w\frac{\partial T}{\partial z}\right) = \frac{1}{\sigma}\left(S^2\frac{\partial^2 T}{\partial x^2} + \frac{\partial^2 T}{\partial z^2}\right) + \frac{M(x)\cos(2\pi t)}{x}, \tag{8}$$

where σ is the Prandtl number, and all variables are dimensionless.

We use the stream function $\psi(u' = -\frac{1}{n_v}\frac{\partial \psi}{\partial z'}, w' = \frac{1}{n_v}\frac{\partial \psi}{\partial x'}$ [24]) that can eliminate the pressure terms in Eqs. (3) and (4), and yield the non-dimensional stream function equation

$$\begin{aligned}&\psi_{tzz} + S^2\psi_{txx} + S^2\mathrm{Gr}\left[(\psi_x\psi_{zzz} - \psi_z\psi_{xzz}) + S^2\left(\psi_x\psi_{xxz} - \psi_z\psi_{xxx}\right)\right]\\ &= \psi_{zzzz} + 2S^2\psi_{xxzz} + S^4\psi_{xxxx} - Ca\tau\psi_{zz} + n_v T_x.\end{aligned} \tag{9}$$

The water surface and sloping bottom are along the same streamline, and their streamline value is setup to zero. The non-dimensionalized boundary conditions are

$$\psi = \psi_x = \psi_{zz} = 0, \qquad T_z = 0 \quad \text{at } z = 0,$$

and

$$\psi = \psi_x = \psi_z = 0, \qquad \left(T_z + S^2 T_x\right)/\sqrt{1+S^2} = 0 \quad \text{at } z = -x. \tag{10}$$

Typical field values for Grashof number ranges from $\mathrm{Gr} \approx 10^7$ for an eddy viscosity of $\nu = 10^{-4}\,\mathrm{m^2\,s^{-1}}$ to $\mathrm{Gr} \approx 10^9$ for a molecular viscosity of $\nu = 10^{-6}\,\mathrm{m^2\,s^{-1}}$ using input solar radiation I_0 of 1,000 $\mathrm{W\,m^{-2}}$ (F04). A typical value for the bottom slope S varies from 10^{-2} to 10^{-3}. If typical field values for Gr and S are adopted, the coefficient $S^2\mathrm{Gr}$ for the convection terms in Eq. (9) may not be smaller than the viscous and temperature gradient on the right-hand side of Eq. (9), i.e., the convective effects cannot be ignored in typical field conditions. F04 pointed out this limitation and defined a valid range for the asymptotic solution. In this study, by considering the vegetative drag, the horizontal velocity is reduced, and the convective effects in Eq. (9) become less important. We will also provide a valid range for the linear asymptotic solutions following the procedures as F04 suggested.

3 Asymptotic solutions

Since no analytic solution for T and ψ can be obtained for Eqs. (8) and (9), we assume the bottom slope S is small, i.e., $S \ll 1$. The small slope appears as S^2 in Eqs. (8) and (9), and the streamfunction ψ and temperature T can thus be expanded as a series of even power for S [25,26]:

$$\psi = \psi^{(0)} + S^2\psi^{(2)} + S^4\psi^{(4)} + \cdots, \quad T = T^{(0)} + S^2T^{(2)} + S^4T^{(4)} + \cdots. \tag{11}$$

After substituting Eq. (11) into Eqs. (8) and (9) and equating the power of S, equations for each order are formed and can be solved recursively.

3.1 Zero-order temperature and horizontal velocity

The zero-order (S^0) temperature equation and streamfunction equation are

$$T_t^{(0)} = \frac{1}{\sigma} T_{zz}^{(0)} + \frac{M(x)\cos(2\pi t)}{x}, \tag{12}$$

$$\psi_{tzz}^{(0)} = \psi_{zzzz}^{(0)} - c_\mathrm{d}\psi_{zz}^{(0)} + n_\mathrm{v} T_x^{(0)}, \tag{13}$$

respectively, where $c_\mathrm{d} = Ca\tau$. The boundary conditions are

$$\psi^{(0)} = \psi_{zz}^{(0)} = T_z^{(0)} = 0 \quad \text{on } z = 0, \tag{14}$$

$$\psi^{(0)} = \psi_z^{(0)} = 0, \qquad T_z^{(0)} = 0 \quad \text{on } z = -x. \tag{15}$$

The initial condition is

$$\psi^{(0)} = T^{(0)} = 0 \quad \text{at } t = 0. \tag{16}$$

Because solar radiation is assumed to be uniformly distributed over the water column, the temperature profiles should also be vertically uniform, i.e., not a function of vertical direction z. By simply integrating Eq. (12) with respect to time t, we can obtain the zero-order temperature solution as

$$T^{(0)} = \frac{M(x)\sin(2\pi t)}{2\pi x}. \tag{17}$$

In this paper, we employ $F(x) = M(x)/x$ to represent the effects of vegetation distribution and topography. As a result, Eq. (13) for the streamline function $\psi^{(0)}$ can be written as

$$\psi_{tzz}^{(0)} = \psi_{zzzz}^{(0)} - c_\mathrm{d}\psi_{zz}^{(0)} + \frac{n_\mathrm{v}\sin(2\pi t)}{2\pi}\frac{\mathrm{d}F(x)}{\mathrm{d}x}. \tag{18}$$

Each term in Eq. (18) from the left to the right represents unsteady inertia, vertical shear, vegetative drag, and buoyancy effects (i.e., horizontal temperature gradient $T_x^{(0)} = \frac{\mathrm{d}F(x)}{\mathrm{d}x}\frac{\sin(2\pi t)}{2\pi}$). By means of Laplace transform, Eq. (18) is transferred to an ordinary differential equation (ODE), which can be then solved easily. In order to transfer the ODE solution from Laplace domain to time domain, the singular points in the ODE need to be identified and Cauchy's residue theorem is applied [27,28]. The streamfunction $\psi^{(0)}$ is solved as follows:

$$\begin{aligned}
\psi^{(0)} = {} & n_\mathrm{v}\frac{\mathrm{d}F(x)}{\mathrm{d}x}\left\{\frac{\sinh\left(z\sqrt{c_\mathrm{d}}\right) - z\sqrt{c_\mathrm{d}}\cosh\left(x\sqrt{c_\mathrm{d}}\right)}{\sinh\left(x\sqrt{c_\mathrm{d}}\right) - x\sqrt{c_\mathrm{d}}\cosh\left(x\sqrt{c_\mathrm{d}}\right)}\left\{\frac{x^2}{2c_\mathrm{d}} - \frac{1}{c_\mathrm{d}^2}\left[\cosh\left(x\sqrt{c_\mathrm{d}}\right) - 1\right]\right\}\right. \\
& - \frac{x\sinh\left(z\sqrt{c_\mathrm{d}}\right) - z\sinh\left(x\sqrt{c_\mathrm{d}}\right)}{\sinh\left(x\sqrt{c_\mathrm{d}}\right) - x\sqrt{c_\mathrm{d}}\cosh\left(x\sqrt{c_\mathrm{d}}\right)}\left\{\frac{x}{c_\mathrm{d}} - \frac{1}{c_\mathrm{d}^2}\sqrt{c_\mathrm{d}}\sinh\left(x\sqrt{c_\mathrm{d}}\right)\right\} \\
& \left. + \frac{1}{2}\frac{z^2}{c_\mathrm{d}} - \frac{1}{c_\mathrm{d}^2}\left[\cosh\left(z\sqrt{c_\mathrm{d}}\right) - 1\right]\right\} \times \frac{\sin(2\pi t)}{2\pi} \\
& - 2n_\mathrm{v}x^3\frac{\mathrm{d}F(x)}{\mathrm{d}x}\sum_{n=1}^{\infty}\frac{1}{\beta_n^2\sin\beta_n}\left[\left(x\sin\left(\frac{\beta_n}{x}z\right) - \beta_n z\cos\beta_n\right)\left(\cos\beta_n + \frac{\cos\beta_n - 1}{\beta_n^2} - \frac{1}{2}\right)\right] \\
& \times \left\{\frac{\left((\beta_n/x)^2 + c_\mathrm{d}\right)\cos(2\pi t) + 2\pi\sin(2\pi t) - \left((\beta_n/x)^2 + c_\mathrm{d}\right)\exp\left(-\left((\beta_n/x)^2 + c_\mathrm{d}\right)t\right)}{\left[\left((\beta_n/x)^2 + c_\mathrm{d}\right)^2 + (2\pi)^2\right]\left(\beta_n^2 + c_\mathrm{d}x^2\right)}\right\},
\end{aligned} \tag{19}$$

where β_n are the positive roots for the equation $\sin\beta_n = \beta_n \cos\beta_n$. If the vegetation is non-uniformed distributed along the horizontal direction, c_d should be a function of x, i.e., $c_\mathrm{d}(x)$.

The horizontal velocity is then given by $u^{(0)}\left(=-\frac{1}{n_\mathrm{v}}\frac{\partial\psi^{(0)}}{\partial z}\right)$, i.e.,

$$
\begin{aligned}
u^{(0)} = &-\frac{\mathrm{d}F(x)}{\mathrm{d}x}\left\{\frac{\sqrt{c_\mathrm{d}}\cosh\left(z\sqrt{c_\mathrm{d}}\right)-\sqrt{c_\mathrm{d}}\cosh\left(x\sqrt{c_\mathrm{d}}\right)}{\sinh\left(x\sqrt{c_\mathrm{d}}\right)-x\sqrt{c_\mathrm{d}}\cosh\left(x\sqrt{c_\mathrm{d}}\right)}\left\{\frac{x^2}{2c_\mathrm{d}}-\frac{1}{c_\mathrm{d}^2}\left[\cosh\left(x\sqrt{c_\mathrm{d}}\right)-1\right]\right\}\right.\\
&-\frac{\sqrt{c_\mathrm{d}}x\cosh\left(z\sqrt{c_\mathrm{d}}\right)-\sinh\left(x\sqrt{c_\mathrm{d}}\right)}{\sinh\left(x\sqrt{c_\mathrm{d}}\right)-x\sqrt{c_\mathrm{d}}\cosh\left(x\sqrt{c_\mathrm{d}}\right)}\left\{\frac{x}{c_\mathrm{d}}-\frac{1}{c_\mathrm{d}^2}\sqrt{c_\mathrm{d}}\sinh\left(x\sqrt{c_\mathrm{d}}\right)\right\}\\
&\left.+\frac{z}{c_\mathrm{d}}-\frac{\sqrt{c_\mathrm{d}}\sinh\left(z\sqrt{c_\mathrm{d}}\right)}{c_\mathrm{d}^2}\right\}\times\frac{\sin(2\pi t)}{2\pi}\\
&+2x^3\frac{\mathrm{d}F(x)}{\mathrm{d}x}\sum_{n=1}^{\infty}\frac{1}{\beta_n\sin\beta_n}\left[\left(\cos\left(\frac{\beta_n}{x}z\right)-\cos\beta_n\right)\left(\cos\beta_n+\frac{\cos\beta_n-1}{\beta_n^2}-\frac{1}{2}\right)\right]\\
&\times\left\{\frac{\left((\beta_n/x)^2+c_\mathrm{d}\right)\cos(2\pi t)+2\pi\sin(2\pi t)-\left((\beta_n/x)^2+c_\mathrm{d}\right)\exp\left(-\left((\beta_n/x)^2+c_\mathrm{d}\right)t\right)}{\left[\left((\beta_n/x)^2+c_\mathrm{d}\right)^2+(2\pi)^2\right]\left(\beta_n^2+c_\mathrm{d}x^2\right)}\right\}.
\end{aligned}
\tag{20}
$$

Without vegetation ($c_\mathrm{d}=0$ and $F(x)=1/x$), the horizontal velocity $u^{(0)}$ becomes the one obtained by FP93, i.e.,

$$
\begin{aligned}
u^{(0)} = &-\frac{1}{96\pi x^2}\sin(2\pi t)\,(z+x)\left(8z^2+zx-x^2\right)\\
&-2x\sum_{n=1}^{\infty}\frac{1}{\beta_n^3\sin\beta_n}\left[\left(\cos\left(\frac{\beta_n}{x}z\right)-\cos\beta_n\right)\left(\cos\beta_n+\frac{\cos\beta_n-1}{\beta_n^2}-\frac{1}{2}\right)\right]\\
&\times\left\{\frac{(\beta_n/x)^2\cos(2\pi t)+2\pi\sin(2\pi t)-(\beta_n/x)^2\exp\left(-(\beta_n/x)^2 t\right)}{\left[(\beta_n/x)^4+(2\pi)^2\right]}\right\}.
\end{aligned}
\tag{21}
$$

The asymptotic solutions $T^{(0)}$and $\psi^{(0)}$ are dependent on vegetation distribution and topographic effects, i.e., $F(x)$.

The exchange flow rate Q'_ex is critical to the evaluation of renewal of water and transport of nutrients or chemical substances in the littoral zones. Following Horsch and Stefan [29], we define the zero-order of dimensionless exchange flow rate $Q_\mathrm{ex}^{(0)}$ per unit width as

$$
Q_\mathrm{ex}^{(0)} = \frac{1}{2}\int_{-x}^{0}\left|u^{(0)}\right|\mathrm{d}z. \tag{22}
$$

3.2 Second-order temperature

The energy equation for the second order $O\left(S^2\right)$, including conduction from the bottom and advection of $T^{(0)}$due to zero-order velocity $u^{(0)}$, is

$$
T_t^{(2)} = \frac{1}{\sigma}T_{zz}^{(2)}+\frac{1}{\sigma}T_{xx}^{(0)}-\mathrm{Gr}u^{(0)}T_x^{(0)}, \tag{23}
$$

subject to the boundary conditions

$$T_z^{(2)} = 0 \quad \text{on } z = 0, \tag{24}$$

$$T_z^{(2)} = -T_x^{(0)} \quad \text{on } z = -x. \tag{25}$$

Equation (25) accounts for the effects of sloping bottom. The asymptotic solution for $T^{(2)}$ can be expressed as $T^{(2)} = T_{\text{cond}}^{(2)} + T_{\text{adv}}^{(2)}$, where

$$T_{\text{cond}}^{(2)} = \frac{1-\cos(2\pi t)}{4\pi^2\sigma}\left(\frac{d^2F(x)}{\mathrm{d}x^2} + \frac{1}{x}\frac{\mathrm{d}F(x)}{\mathrm{d}x}\right) + \frac{1}{\pi x}\frac{\mathrm{d}F(x)}{\mathrm{d}x}\sum_{n=1}^{\infty}(-1)^n\cos\left(\frac{n\pi z}{x}\right) \times \frac{(n\pi/x)^2\sin(2\pi t) + 2\pi\sigma\left[\exp\left(-(n\pi/x)^2 t/\sigma\right) - \cos(2\pi t)\right]}{(n\pi/x)^4 + (2\pi\sigma)^2} \tag{26}$$

is the horizontal conduction due to the sloping bottom, and

$$T_{\text{adv}}^{(2)} = \text{Gr}\sigma x\sum_{m=1}^{\infty}\left\{\left[a_m(x,t) + \frac{4(-1)^m x^4}{\pi}\left(\frac{\mathrm{d}F(x)}{\mathrm{d}x}\right)^2\sum_{n=1}^{\infty}b_{mn}(x,t)\,c_{mn}(x,t)\right]\cos\frac{m\pi z}{x}\right\} \tag{27}$$

is the correction because of the advection (F04). The parameters a_m, b_{mn}, and c_{mn} in Eq. (27) are given in Appendix. $F(x)$ that denotes effects of vegetation distribution and sloping bathymetry appears in both $T_{\text{cond}}^{(2)}$ and $T_{\text{adv}}^{(2)}$. For the case without vegetation, i.e., $c_{\text{d}} = 0$, and $F(x) = 1/x$, the solution for second-order temperature becomes the same as Eqs. (A1)–(A4) in F04. The dimensionless horizontal advective heat transfer per unit is given by $q = S^2\int_{-x}^{0} u^{(0)}T^{(2)}\mathrm{d}z$. The zero-order temperature, constant along the water column, will not contribute to q (F04).

4 Results and discussion

4.1 Zero-order asymptotic solutions

The results derived in the previous section offer the horizontal velocity under different vegetation distributions. The discussion here first focuses on uniform distributions of rooted emergent vegetation regimes, which have a constant value of $M(x)$ in Eq. (17), i.e., $M(x) = c$, where c is a constant associated with the vegetation height and the numbers of vegetation leaves. Since $F(x) = M(x)/x$, $\frac{\mathrm{d}F(x)}{\mathrm{d}x}$ that is proportional to temperature gradient (forcing) is equal to $\frac{\mathrm{d}F(x)}{\mathrm{d}x} = -\frac{c}{x^2}$. Here, the vegetation is assumed to be rooted, emergent, and very close to the water surface. In addition, the vegetation has no leaf, i.e., the cross-sectional area of the stem is constant vertically. The emergent vegetation blocks part of solar radiation penetrating into the water, but meanwhile, the volume occupied by water is also decreased. For example, 0.25 % of vegetation (99.75 % occupied by water) blocks 0.25 % of solar radiation, i.e., allowing 99.75 % solar radiation into 99.75 % volume occupied by water. Therefore, the volumetric absorptions of solar radiation in the water body with 0.25 % vegetation and no vegetation are identical. The constant c is then equal to 1, and the temperature magnitudes and profiles for 0.25 % vegetation are the same as for the case without vegetation, but additional vegetative drag affects the flow field. In the field, the leaves of the vegetation typically have

larger area than the stem cross-sectional area, in which case, the constant c may not be 1. In this study, we choose the diameter of vegetation stem d of 0.6 cm commonly found in typical field conditions [20] as an example to discuss the vegetative effect on thermally driven flow.

The horizontal velocity with vegetative drags denoted by c_d is embedded almost in every term of Eq. (20). On the contrary, without vegetation, the horizontal velocity (Eq. (21)) can be separated as viscous (the first term on the right-hand side), and inertia and transient responses (the second term on the right-hand side) as FP93 indicated. Equation (21) shows that in shallow water ($x \ll 1$), the first term on the right-hand side of Eq. (21) is more important, i.e., viscosity is mainly balanced with buoyancy. In deep water ($x \gg 1$), however, the second term on the right-hand side of Eq. (21) is greater, i.e., inertia and transient effects are significant. Therefore, the vegetative drag has impacts both on viscous and inertia responses (Eq. (20)).

The e-folding time t_e (decreasing a quantity by a factor of e, i.e., Napier's constant) for the transient term in Eqs. (20) and (21) is

$$t_\mathrm{e} = \frac{1}{(\beta_1/x)^2 + c_\mathrm{d}} \approx \frac{1}{20.19/x^2 + c_\mathrm{d}}, \tag{28}$$

which is a function of x and c_d. Because c_d is always positive, t_e within vegetation is smaller than that without vegetation, i.e., the transitional stage within vegetation is shorter than that without vegetation. The ratios of e-folding time with 0.25 % vegetation to no vegetation in shallow water ($x = 0.25$), intermediate depth ($x = 1$), and deep water ($x = 5$) are 0.961, 0.03, and 0.06, respectively. This means that the e-folding time is significantly reduced by the presence of vegetation and decreased still further more in deep water than in shallow water. At the same location x, denser vegetation, i.e., larger c_d, has a smaller e-folding time. Horizontal velocity thus experiences a shorter transient stage from the onset of the flow and assumes purely periodic patterns rapidly due to the presence of the emergent vegetation. Also the vegetative drag c_d is included in the denominator of the second term on the right-hand side of Eq. (20). As the vegetation becomes denser, i.e., the larger the c_d, the smaller the second term on the right-hand side of Eq. (20) becomes, and thus the inertial and transient effects are less important within the rooted emergent vegetation.

In order to discuss dominant physical mechanisms at different water depths, Fig. 2 depicts the time evolution ($t = 0$–3) of the viscous ($u_{zz}^{(0)}$), the inertia ($u_t^{(0)}$), the horizontal pressure gradient ($-p_x^{(0)}$) from buoyancy, the vegetative drag ($-c_\mathrm{d}u^{(0)}$), and the horizontal velocity ($u^{(0)}$) at the water surface in the zero-order dimensionless horizontal momentum equation shown below:

$$u_t^{(0)} = -p_x^{(0)} - c_\mathrm{d}u^{(0)} + u_{zz}^{(0)}. \tag{29}$$

Each term in Eq. (29) is obtained by integrating Eq. (13) with respect to the z direction. The horizontal velocity can be correlated to the inertia term (acceleration a) by the formula of $u = \int a\mathrm{d}t$, and therefore, the horizontal velocity u and inertia term a are always out of phase. Within vegetation, the viscous term in shallows ($x = 0.25$, Fig. 2a) is dominant and balanced with the buoyancy (i.e., pressure gradient). Effects of the vegetative drag are small within 0.25 % vegetation. For the case of without vegetation, viscosity is also dominant in shallows (Fig. 2d) as FP93 mentioned. Although the pressure gradient is larger in shallows, the larger viscous effect counteracts the pressure gradient. Consequently, the resulting inertia is too small to generate greater horizontal velocity. The pressure gradient and zero-order horizontal velocity $u^{(0)}$ are at the same phase, which means that flow will respond immediately to the change of the pressure gradient. For the limiting case of $x \to 0$, $u^{(0)}$ reverses

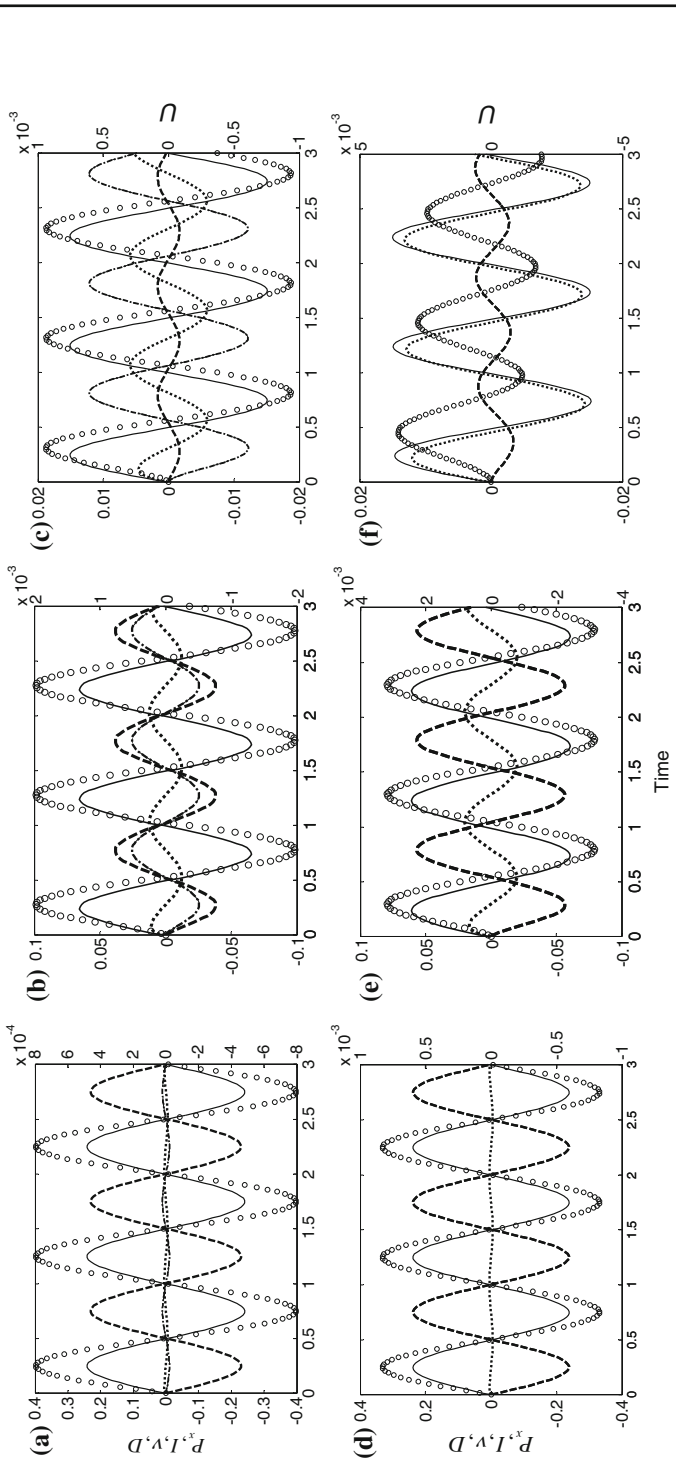

Fig. 2 Different terms and horizontal velocities at the water surface ($z = 0$) in the vegetation densities of 0 and 0.25 % for the three cycles. **a** $x = 0.25$, $\phi = 0.25$ %; **b** $x = 1$, $\phi = 0.25$ %; **c** $x = 5$, $\phi = 0.25$ %; **d** $x = 0.25$, $\phi = 0$ %; **e** $x = 1$, $\phi = 0$ %; and **f** $x = 5$, $\phi = 0$ %. *Left axis* denotes dimensionless pressure gradient, inertial, viscosity, and drag terms; *Right axis* represents dimensionless horizontal velocity; *Solid line* the pressure gradient P_x; *dotted line* the inertia I; *dashed line* the viscosity ν; *dash dotted line* the drag D, and *open circle* the horizontal velocity U

instantaneously to the reversal of the pressure gradient (FP93). Because e-folding time is small for smaller x values (Eq. (28)), the transient behavior is too short to be observed in shallows, and the flow shows a very regular pattern, i.e., large-time behavior is achieved rapidly.

At the intermediate depth ($x = 1$, Fig. 2b, e), vegetative drag becomes more important but still less than the viscous effect. Since inertia is reduced by both viscosity and vegetative drag, the induced horizontal velocity is smaller than that without vegetation. As water becomes deeper, both viscous effects and pressure gradient decrease; however, the viscous effect decreases faster than the pressure gradient. The induced inertia turns to become more important as the water depth increases. Also, the phases of pressure gradient and horizontal velocity are not the same, both in the cases with and without vegetation. The time lag with vegetation is shorter than that without vegetation. If the vegetation becomes denser, then the vegetative drag will exceed the viscosity at this depth, and the time lag between horizontal velocity and pressure gradient becomes less pronounced as well.

In deep water ($x = 5$, Fig. 2c, f), vegetative drag becomes more important than the viscosity and significantly reduces the magnitudes of inertia as well as horizontal velocity. Within vegetation, the time lag between the reversal of the horizontal velocity and pressure gradient is small. Without vegetation, larger inertias arising from smaller viscous effects leads to an apparent time-lag phenomenon between the reversal of the horizontal velocity and the pressure gradient. The inertia term is positive from $t = 0$ to $t \approx 0.5$, and in turn, the maximum horizontal velocity occurs at $t \approx 0.5$, corresponding to the largest positive area under the curve of the inertia term with respect to time. The time lag between the reversal of the flow and the pressure gradient is up to 0.25, i.e., a quarter of the forcing period as FP93 described. In deeper water and without vegetation, the inertia is approximately in the same phase as the pressure gradient but is out of phase with the horizontal velocity. The positive horizontal velocity is larger than the negative horizontal velocity at the onset of forcing initiated and then gradually becomes equal to the latter as time increases [17].

4.2 Transient velocity behavior within vegetation

Figure 3 shows streamlines at various times within 0.25 % vegetation. At $t = 1$, because of the residual inertia from the cooling period, counterclockwise circulation is found over the entire flow field. At $t = 1.01$, shortly after the pressure gradient reverses, a zero streamline that intersects the water surface in the flow domain divides the flow into two opposite circulation regions. In the areas close to the tip, the circulation is first reversed by the pressure gradient, and a propagating front emerges from the tip to the deep water. In the remaining regions, an opposite propagating front that flows from the deep water to the shallow water still remains. The position of zero surface velocity keeps moving to deep water as time progresses until the entire flow field is completely reversed at $t = 1.07$. The flow field continues to accelerate from the shallow water to the entire flow field. The flow patterns are very similar to the large-time behavior without the presence of vegetation (see Fig. 4 in FP93). For the streamlines without vegetation, the larger inertia maintains the counterclockwise circulation at $t = 1.12$ at the intermediate water depth, and two clockwise propagating fronts, one in shallow water, and one in deep water are evident (see Fig. 6 in FP93). The vegetative drag reduces the inertia of the circulation and causes the counterclockwise circulation to survive shorter than the circulation without vegetation in the flow field.

To further elucidate the physical mechanisms at various water depths, we balanced one among the terms of viscous, inertia, and vegetative drag with temperature gradient (buoyancy) in Eq. (13) to obtain the solutions for the limiting cases. The zero-order velocity for the case of

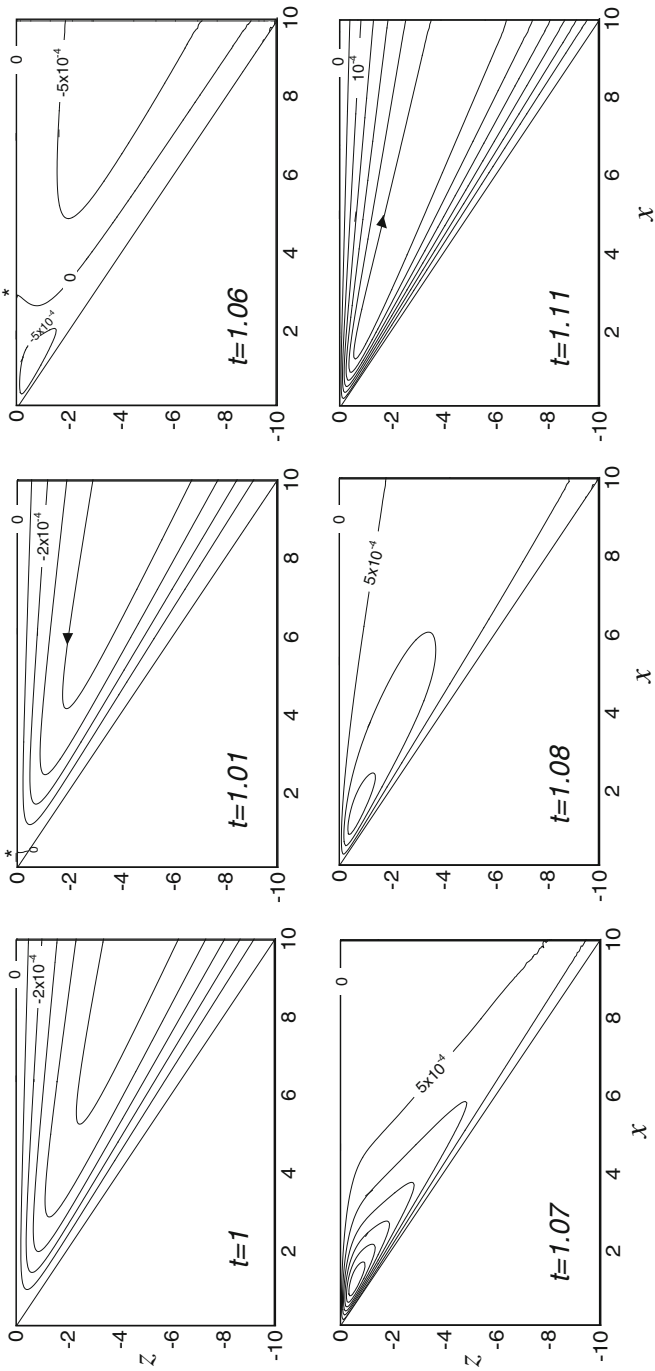

Fig. 3 Streamlines for various times within 0.25 % vegetation. The *numbers* denote the values of the streamlines, and the *asterisk* indicates the position of zero surface velocity

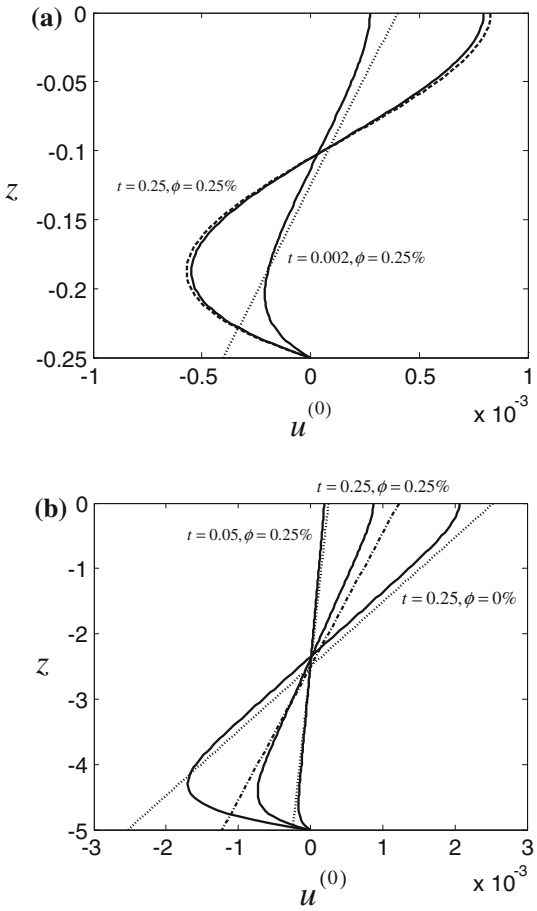

Fig. 4 Horizontal velocity profiles within and without vegetation for various times in shallow and deep water. *Solid line* full solution of horizontal velocity, *dashed line* viscous-limiting of horizontal velocity, *dotted line* inertia-limiting of horizontal velocity, and *dash dotted line* drag-limiting of horizontal velocity). In (**a**), the horizontal velocity profiles at $t = 0.002$ are 100 times larger than the actual values. In (**b**), the horizontal velocity profiles at $t = 0.05$ are two times larger than the actual values

only including viscosity $u_{\mathrm{v}}^{(0)}$, inertia $u_{\mathrm{i}}^{(0)}$, or vegetative drag $u_{\mathrm{d}}^{(0)}$ to balance with temperature gradient is given by

$$u_{\mathrm{v}}^{(0)} = \frac{\mathrm{d}F(x)}{\mathrm{d}x}\frac{\sin(2\pi t)}{96\pi}(z+x)\left(8z^2+zx-x^2\right) \tag{30}$$

$$u_{\mathrm{i}}^{(0)} = \frac{1}{8\pi^2}\frac{\mathrm{d}F(x)}{\mathrm{d}x}(2z+x)\left[\cos(2\pi t)-1\right] \tag{31}$$

$$u_{\mathrm{d}}^{(0)} = -\frac{\sin(2\pi t)}{4\pi c_{\mathrm{d}}}\frac{\mathrm{d}F(x)}{\mathrm{d}x}(2z+x)\,. \tag{32}$$

For the inertia- and drag-limiting cases, the bottom velocity is not equal to zero in the absence of viscosity. Only the velocity profiles derived from limiting cases close to the full solution are shown, and the velocity profiles from the limiting cases that deviate considerably from the full solution are excluded in Fig. 4.

The horizontal velocity profiles are initially balanced by the inertia and horizontal pressure gradient and then gradually affected by viscosity and vegetative drag. At short periods of time, the horizontal velocity profiles can be characterized as a straight line, corresponding to the inertia-limiting velocity profiles given by F04 except the regions near the boundary,

where viscosity prevails (Fig. 4). The inertia-dominant region is based on the time scale when viscosity diffuses into the entire water column, i.e., $t_v \sim x^2$, and the time for vegetative drag to become dominant is $t_d \sim (Ca\tau)^{-1}$ as suggested by Zhang and Nepf [9]. For 0.25 % vegetation with diameter of 0.6 cm, $t_d \sim 0.078$ compares with $t_v \sim 0.0625$ at $x = 0.25$, $t_v \sim 1$ at $x = 1$, and $t_v \sim 25$ at $x = 5$. This means that the effect of vegetative drag surpasses the viscous effect as the water depth increases. According to experiments conducted in a constant-depth and steady light source conditions, Zhang and Nepf [9] suggested that the flow becomes vegetative drag dominant as the time increases. With 0.25 % vegetation, the inertias at $x = 0.25$, and 5 are dominant and balanced by buoyancy until $t = 0.002$ and 0.05 (Fig. 4), respectively; whereas, without vegetation, the time for inertia-dominance at $x = 0.25,$ and 5 is longer, and can be up to $t = 0.25$ for $x = 5$ (F04). Figure 4a also shows that as the time increases, the viscous effect in shallow water ($x = 0.25$) is more important than the vegetative drag, and the horizontal velocity profiles can be simplified as a viscous/buoyancy balance (Eq. (30)) given by F04. Within 0.25 % vegetation, the slight differences between the horizontal velocity profiles and viscous-dominated profiles shown in Fig. 4a are due to the impact of vegetative drag. As vegetation becomes denser, the effect of vegetative drag becomes obvious in shallow water.

The straight-line velocity profiles (Eq. (32)) are the feature of the drag-dominated regime as Tanino et al. [21] indicated in the lock-exchange experiment. When the vegetation is denser, i.e., with a larger c_d, the slope of the velocity profiles becomes steeper. In deep water and without vegetation, the flow field is dominated by the inertia at the beginning as F04 described, as also shown in Fig. 4b ($t = 0.25, \phi = 0\,\%$). As the time increases, the entire flow field will be eventually affected by viscosity. Within vegetation, the inertia is prevalent for a very short time (Fig. 4b, $t = 0.05$, $\phi = 0.25\,\%$), and the vegetative drag then becomes dominant. As a result, the horizontal velocity profiles can be represented by drag-limiting velocity profiles (Fig. 4b, $t = 0.25$, $\phi = 0.25\,\%$). Near the boundary, the deviations between the full asymptotic, inertia and drag-dominant solutions are considerable because of lack of the viscous boundary layers. In Fig. 4b, the distance from the bottom to the point where velocity profiles turn to the opposite direction can be regarded as the region affected by viscosity. It is noted that with the presence of vegetation, the viscosity-dominated regions shrink, and the vegetative drag suppresses the growth of the boundary layer (Fig. 4b, with $t = 0.25, \phi = 0\,\%$, and $0.25\,\%$). Based on the scaling analysis (see Sect. 2.2), the ratio of vegetative drag to inertial terms is $Ca\tau$. When $Ca\tau \ll 1$, the vegetative effect can be neglected. Assuming a vegetation diameter of 0.6 cm, the corresponding critical vegetative density ϕ_{critical} to satisfy $Ca\tau = 1$ is $\sim 0.069\,\%$. The vegetation density larger than ϕ_{critical} implies that the flow field will be affected by the presence of vegetation.

4.3 Large-time velocity behavior within vegetation

Large-time behavior means disappearance of the transient effect, i.e., exponent term becomes zero in Eqs. (19), (20), and (21). Due to vegetation, transient time becomes much shorter than that without vegetation. Streamlines shown in Fig. 3 are very similar to the streamlines for the large-time behavior. Figure 5 illustrates a series of velocity profiles at the water depth of 1 near the time when the pressure gradient is reversed. At this water depth, with 0.25 % vegetation, horizontal velocity is reversed at $t \approx 0.53$, i.e., time lag of ~ 0.03; while horizontal velocity without vegetation reverses at $t \approx 0.55$, i.e., time lag of ~ 0.05. In both cases, three-layer structures of the flow velocities are observed. In shallow water (depth of 0.25), the time lags with and without 0.25 % vegetation are similar and very small, being less than 0.005, i.e., the circulation is approximately in phase (lock phase) with the pressure gradient. As water depth

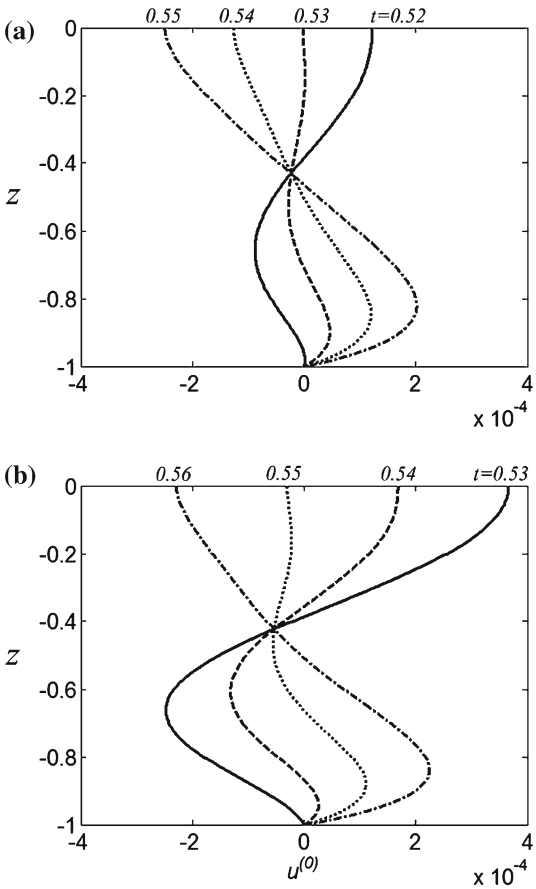

Fig. 5 Velocity profiles near the time when the pressure gradient is reversed (spin-time effect) at the depth of 1: **a** $\phi = 0.25\,\%$ and **b** $\phi = 0\,\%$

increases, the viscous effect becomes less important, leading to larger inertia, and the time lags between the reversal of circulation and the pressure gradient become pronounced. In deep water (water depth of 5), for 0.25 % vegetation, the flow is reversed between $t = 0.56$ and 0.57. The time lag t_{lag} is reduced by four times in comparison with the flow without vegetation ($t_{\text{lag}} = 0.2$–0.23 without vegetation and $t_{\text{lag}} = 0.06$–0.07 with vegetation). As vegetation population becomes denser, the time lag becomes smaller. For instance, for 0.5 and 1 % vegetations, the time lags at $x = 1$ are $\sim$0.025 and $\sim$0.005, respectively.

4.4 Surface velocity and exchange flow rates

Figure 6 provides contours of surface velocity $u|_{z=0}$ over $(x - t)$ domain after the forcing is initiated. Because of vegetative drag, the transient period of surface velocity becomes smaller, and the patterns of surface velocity are similar in the first four cycles, i.e., the flow reaches the large-time behavior. In addition, the time lag between the reversal of velocity and the pressure gradient in shallow water is close to zero. In deep water ($x = 10$), however, the circulation is reversed at $t \sim 0.55$, i.e., time-lag of $\sim$0.05 (Fig. 6a). Without vegetation, the time lag in shallow water is also close to zero, but in deep water ($x = 10$), the flow would experience an adjustment time until the flow becomes purely periodic [17]. In deep

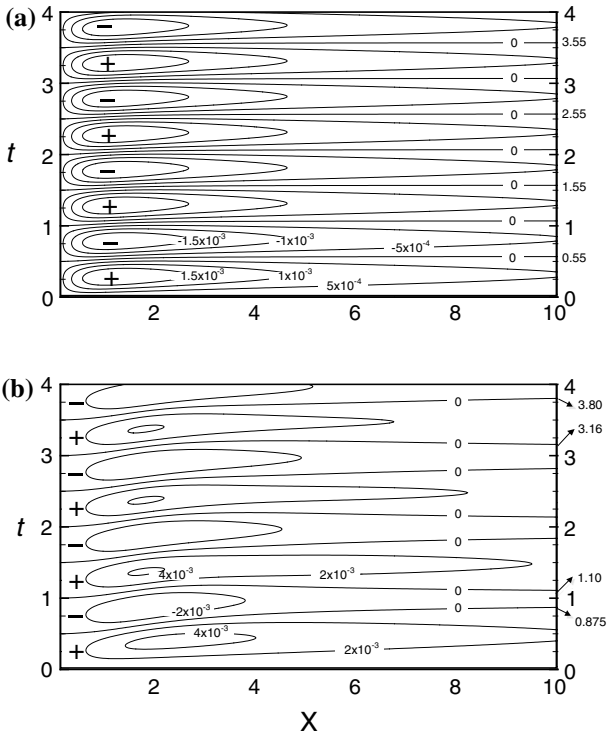

Fig. 6 Contours of surface horizontal velocity $u|_{z=0}$ in the $(x-t)$ domain for **a** $\phi = 0.25\,\%$; and **b** $\phi = 0\,\%$. The *small numbers labeled on the right y-axis* represent the time for the reversal of the circulations

water, the time lag dramatically changes during the adjustment time. In the first half cycle, the circulation at $x = 10$ is revered at $t = 0.875$, i.e., $t_{\text{lag}} = 0.375$, and the reversed flow due to the cooling period only lasts for a short period, i.e., the flow is reversed again at $t = 1.10$, i.e., $t_{\text{lag}} = 0.10$. At the transient stage (or adjustment time), the positive surface velocity (surface flow from the tip to offshore) lasts longer at the beginning, and the negative surface velocity (surface flow from deep water to shallow water) gradually becomes larger and finally becomes equal to the positive surface velocity when the large-time behavior is achieved. After four cycles, however, the positive velocity is still larger than the negative velocity, as shown in Fig. 6b, i.e., the large-time behavior has not been reached yet. As the time increases, the time-lag t_{lag} due to the heating and cooling periods gradually becomes similar, and finally, it becomes identical, which is $t_{\text{lag}} = 0.25$ as FP93 indicated.

It is also noted that as a result of vegetation, locations of maximum or minimum surface velocity move closer to the tip in comparison with the no-vegetation case. With $0.25\,\%$ vegetation, the locations of maximum and minimum velocity occur at $x \sim 1.2$. On the other hand, the locations for the maximum and minimum velocity without vegetation are not equal at the transient stages. At the beginning, the locations of the maximum and minimum horizontal velocity during heating and cooling periods are at $x \sim 2.5$ and 2, respectively. As the time increases, the locations for extreme velocity gradually approach to $x \approx 2$ as FP93 indicated.

According to the horizontal velocity profiles, the exchange flow rate Q can be estimated by means of Eq. (22). In Fig. 7, the exchange flow rate is proportional to the water depth

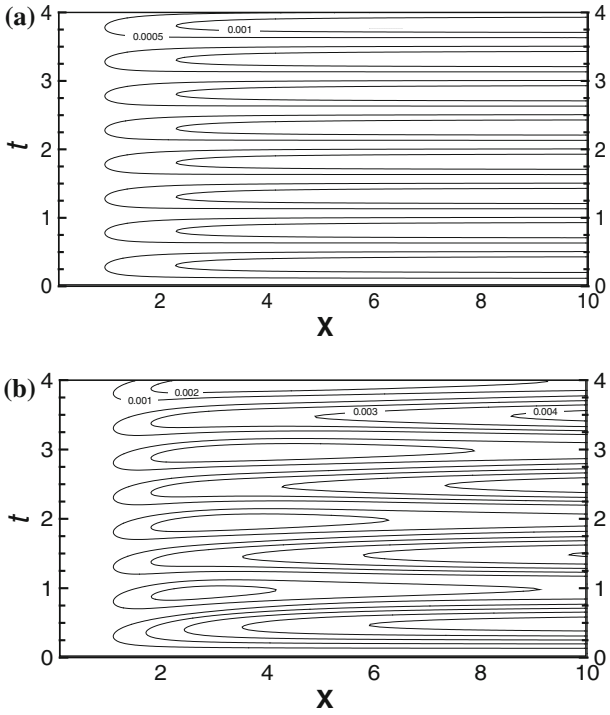

Fig. 7 Contours of exchange flow rates in the $(x - t)$ domain for **a** $\phi = 0.25\,\%$ and **b** $\phi = 0\,\%$

both the regimes of within and without vegetation, corresponding to the findings from several previous studies [19,30,31]. In shallow water, the exchange flow rate in vegetation is smaller and approximately varies with $\sin(2\pi t)$, i.e., the maximum exchange flow rate occurring at $t = 0.25$ and $t = 0.75$ (Fig. 7a).

As expected, when water depth increases, the inertia effects lag the occurring of the maximum exchange flow rate to $t = 0.30$ and 0.80. Without vegetation, at the transient stage, the positive surface velocity from daytime heating is larger than the negative surface velocity from cooling processes. As a result, the maximum exchange flow rates during the heating period are greater than that during the cooling period at the initial stage (or adjustment time). As the time progresses, the occurring times of the maximum exchange flow rates in heating and cooling periods gradually are the same, i.e., at $t = 0.5$ and 1 when the transient effects vanish. On comparison with Fig. 7a, b, it is observed that the presence of vegetation reduces the exchange flow rate, regulates the phase of exchange flow rate with the pressure gradient, and also decreases the transient time for the exchange flow rate to reach the large-time behavior.

4.5 Vegetation distribution

In typical field conditions, spatial variations of nutrients, light climate, and hydrodynamic conditions commonly lead to nonuniform distribution of the horizontal vegetation, which changes the horizontal distribution of solar radiation impinging on the water body. In this study, $M(x)$ represents the distribution of solar radiation along the horizontal direction. If

vegetation density linearly increases or decreases along the horizontal direction, then $M(x)$ for simplicity can be expressed as a linear function, which is $M(x) = a + bx$ where a, b are the variables related to vegetation features such as vegetation height, the number of vegetation leaves, and the increasing or decreasing rates of vegetation density along the horizontal direction. The forcing, i.e., temperature gradient, is proportional to $\frac{\mathrm{d}}{\mathrm{d}x}[\frac{M(x)}{x}]$, which is equal to $-\frac{a}{x^2}$. In comparison with temperature gradient $T_x^{(0)}$ from no-vegetation $\left(T_x^{(0)} \propto -\frac{1}{x^2}\right)$ and uniform-distributed vegetation ($T_x^{(0)} \propto -\frac{c}{x^2}$, condirions see Sect. 4.1), patterns of temperature profiles are similar, but its magnitude is reduced depending on the parameter a. The circulation patterns are also affected by c_d in Eqs. (19) and (20), which is a function of x. However, the linearly increasing or decreasing c_d values may not lead to distinguished variations of circulation patterns over the flow domain. Here, we focus on dramatic vegetation distribution, i.e., vegetation grows in one side of the flow domain and sharply disappears in the other side of the flow domain. The extreme conditions such as vegetation occupying half of the entire domain, and open water in the other half domain commonly found in field [7,9] can result in additional heat drivers in Eq. (13). In this study, a Heaviside function is adopted to describe the distribution of solar radiation $M(x)$ for one-side vegetation (ϕ_0) and one-side open water ($\phi = 0\,\%$), which is

$$M(x) = (1 - B) + \frac{B}{1 + \exp\left[-2k\left(\frac{x}{L_x} - 0.5\right)\right]}, \tag{33}$$

where B is the blockage percentage of solar radiation by vegetation and B ranges between 0 (all solar radiation pass through vegetation) and 1 (all solar radiation is blocked by vegetation), and L_x is the dimensionless length of the flow domain, k means the sharpness of the transition of solar radiation from vegetation to open water, and the sign of k values determines the vegetation growth in shallow or deep water.

The solid volume fraction of vegetation ϕ $(= 1 - n_\mathrm{v})$ is:

$$\phi(x) = \phi_0 \cdot G(x), \tag{34}$$

where ϕ_0, the solid volume fraction of vegetation in the vegetation side, and

$$G(x) = \left[\frac{1}{1 + \exp\left(2k\left(\frac{x}{L_x} - 0.5\right)\right)}\right].$$

If the vegetation is emergent only at several centimeters from the water surface, then this kind of emergent vegetation causes identical temperature variations relative to the case without vegetation. Once the emergent vegetation like reed is tall with height of 2–3 m above the water surface, small amounts of high reeds can even block averagely 85 % the incident solar radiation [7]. The vegetation-shading effect causes little solar radiation penetrating into water body and leads to lower temperature in dense vegetation areas than no or sparse vegetation areas during daytime. If the dense vegetation grows in shallow water, commonly found in the field, the shading effect can produce lower water temperature which contradicts the temperature fields due to the topographic effect, and may change the direction of the temperature gradient as well as the circulation patterns. By means of Eq. (33), the term $\frac{\mathrm{d}}{\mathrm{d}x}\left[\frac{M(x)}{x}\right]$ associated with horizontal temperature gradient can be obtained as

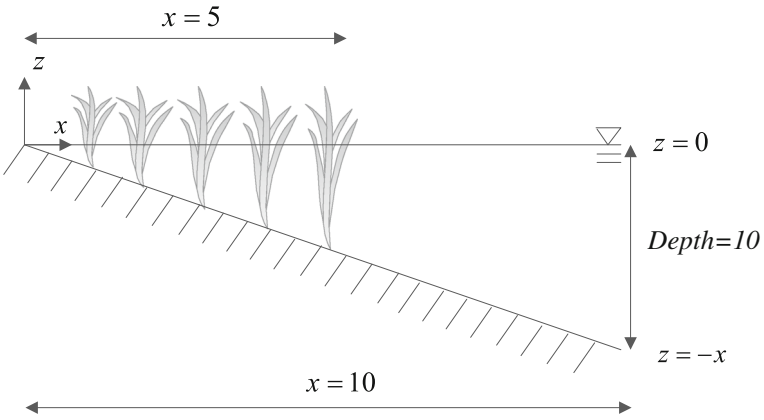

Fig. 8 Schematics of vegetation in shallow water and open in deep water. The domain dimensionless length L_x is set to 10, and the tall vegetation grows until $x = 5$

$$\frac{\mathrm{d}}{\mathrm{d}x}\left[\frac{M(x)}{x}\right] = -\frac{(1-B)}{x^2} - \frac{1}{x^2}\frac{B}{1+\exp\left(-2k\left(\frac{x}{L_x}-0.5\right)\right)} + \frac{2Bk\exp\left(-2k\left(\frac{x}{L_x}-0.5\right)\right)}{xL_x\left[1+\exp\left(-2k\left(\frac{x}{L_x}-0.5\right)\right)\right]^2}. \tag{35}$$

In Eq. (35), physical meanings for the three terms on the right-hand side are described as follows. The first term on the right-hand side represents the topographic effect. The second term indicates the adjustment of the topographic pressure gradient, because the sharp vegetation distribution alters temperature distribution. The third terms on the right-hand side means the temperature gradient produced by the sharp vegetation distribution. The magnitudes of these terms can be used to evaluate the dominance of topographic or vegetation shading effects at different locations.

Figure 8 illustrates a schematic for one extreme condition, which is for $k > 0$, vegetation in shallow water, and open in deep water. Assume the domain length L_x as 10, and the vegetation density to be 0.25 %; then, the interface between vegetation and open water is at the center line of $x = 5$. In order to examine the interplay between the vegetation-shading and topographic effects, exchange flow rates at the centerlines of the flow domains (vegetation/water interface) are compared, including the two extreme cases: (i) vegetation in shallow water, and open in deep water; and (ii) open in shallow water, and vegetation in deep water with different blockages B and sharpness k. For the case of vegetation in shallow water, and open in deep water (Fig. 9a), i.e., $k > 0$, as the blockage B becomes larger, the first and second terms on the right-hand side of Eq. (35) reduce, but the third term becomes larger. Thereby, a critical blockage B_{critical} that results in zero exchange flow rate at the centerline of the domain can be found. Furthermore as the sharpness k increases, B_{critical} will decrease. For example, $k = 5$ leads to $B_{\text{critical}} = \frac{4}{7}$, and $k = 10$ yields $B_{\text{critical}} = \frac{1}{3}$. Interestingly, $k = 1$ cannot result in zero exchange flow rate at the centerline but decreases the exchange flow rates as the vegetation blockage B increases. The critical blockage B_{critical} identifies the regions dominated by topographic or shading effects. For the ranges of $B < B_{\text{critical}}$, circulation patterns are mainly determined by the forcing generated from the sloping bottom but reduced by vegetation shading. Consequently, circulation patterns are the same as those in no vegetation or uniform-

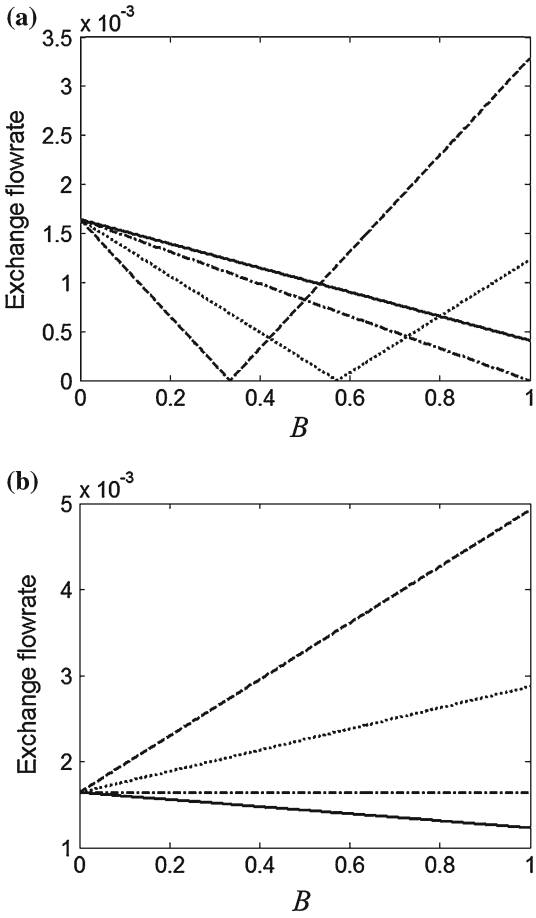

Fig. 9 Dimensionless exchange flow rates with different blockage B and sharpness k. **a** Vegetation in shallow water, and open in deep water; and **b** open in shallow water, and vegetation in deep water. *Solid line* $k = \pm 1$; *dash dotted line* $k = \pm 2$; *dotted line* $k = \pm 5$; and *dashed line* $k = \pm 10$

distributed vegetation cases, i.e., during daytime, circulation flowing from shallow water to deep water along the water surface, and uphill over the sloping bottom. On the contrary, when $B > B_{\text{critical}}$, the vegetation-shading effect exceeds the topographic effect, and the flow patterns become opposite to that in the case of $B < B_{\text{critical}}$. When the blockage B is much larger than B_{critical}, the induced temperature gradient becomes greater, causing larger circulation and exchange flow rates (Fig. 9a).

For the other extreme case, i.e., open in shallow water, and vegetation in deep water ($k < 0$), the topographic and vegetation shading effects generate horizontal temperature gradient along the same direction. For $k = -5$ and -10, exchange flow rates increase linearly as the blockage B becomes larger. However, for $k = -2$ and -1, the increases of vegetation blockage keep the exchange flow rate as a constant or even decrease the exchange flow rate. This is because smaller absolute k values in Eq. (35) not only cause a milder transition but also affects to a wider extent on the distribution of solar radiation. The mild decreasing input solar radiation along the horizontal direction alters the temperature distribution over the entire domain, which means that the water temperature in shallow water is lower than that in deep water during daytime. The temperature gradient from the sloping bathymetry is reversed, and the temperature gradient gained from the vegetation shading is not large enough to compensate the reduction due to the topographic effect.

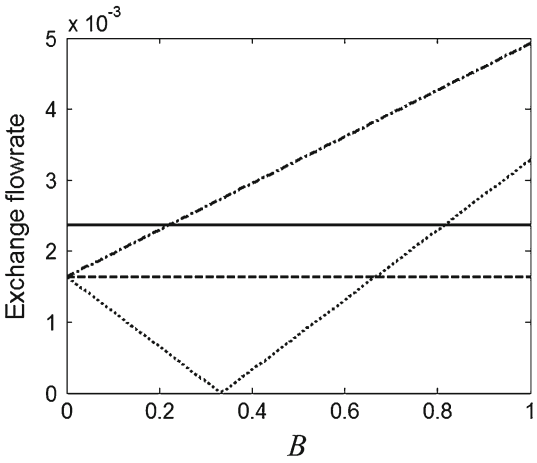

Fig. 10 Exchange flow rates at the center line of four cases with different blockages B. *Solid line* denotes case (i): no vegetation; *dashed line* represents case (ii): 0.25 % vegetation; *dotted line* means case (iii): vegetation in shallow water and open in deep water; and *dash dotted line* denotes case (iv): open in shallow water, and vegetation in deep water

Figure 10 provides the comparisons of exchange flow rate for four scenarios: (i) no vegetation, (ii) 0.25 % vegetation, (iii) vegetation in shallow water and open in deep water, and (iv) open in shallow water, and vegetation in deep water at centerline and with absolute sharpness $|k|$ of 10. The extreme vegetation distributions for both the cases of (iii) and (iv) can result in larger exchange flow rates than the case without any vegetation. Specifically, for case (iii), it also can lead to a smaller exchange flow rate than the case of uniform-distributed vegetation. In the above mentioned four cases, we assume a sharp change of the uneven vegetation and heat distribution, which can generate temperature gradient much larger than the one from the topographic effect. Therefore, even the vegetation can reduce the circulation, the additional thermal driving force produced by the sharp vegetation distribution causes larger exchange flow rates than those in a fully open water domain.

The circulation patterns are mainly determined by the sharpness coefficient k and blockage B. Figure 11 provide an example for large-time streamlines at $t = 0.2$ under different conditions. Without vegetation, only the circulation in shallows is reversed, but it remains counterclockwise in deep water (Fig. 11a). With 0.25 % uniform-distributed vegetation, the circulation has been completely reversed at $t = 0.2$ (Fig. 11b). For the case of open in shallow water, and vegetation in deep water (Fig. 11c), the vegetation shading intensifies the topographic effect to generate strong circulation at the water–vegetation interface ($x = 5$). In shallow water, a residual counterclockwise circulation from the cooling period is revealed at $x \approx 4$. Meanwhile, the circulation is already reversed in shallow water and in very deep water. In Fig. 11d (vegetation in shallow water, and open in deep water), the small reduction of solar radiation does not significantly change the circulation patterns. In shallow water with vegetation, the circulation has been reversed; however, the residual circulation still remains in open and deep water. As the blockage value B increases, the regions affected by the vegetation–water interface emerge. In Fig. 11e, two vertical zero streamlines are found at $x \approx 4.9$ and 5.1. Also, within this region ($x = 4.9$–5.1), circulations affected by the vegetation shading always perform opposite patterns to those in shallow and deep water. The regions with two vertical streamlines become even wider when the blockage B is equal to 0.85 (Fig. 11f). However, for very shallow and deep water, the circulations are still the same as those within vegetation or in open water, respectively. Only the central portion is affected by the vegetation distribution, and the size of the affected regions is determined by the blockage B.

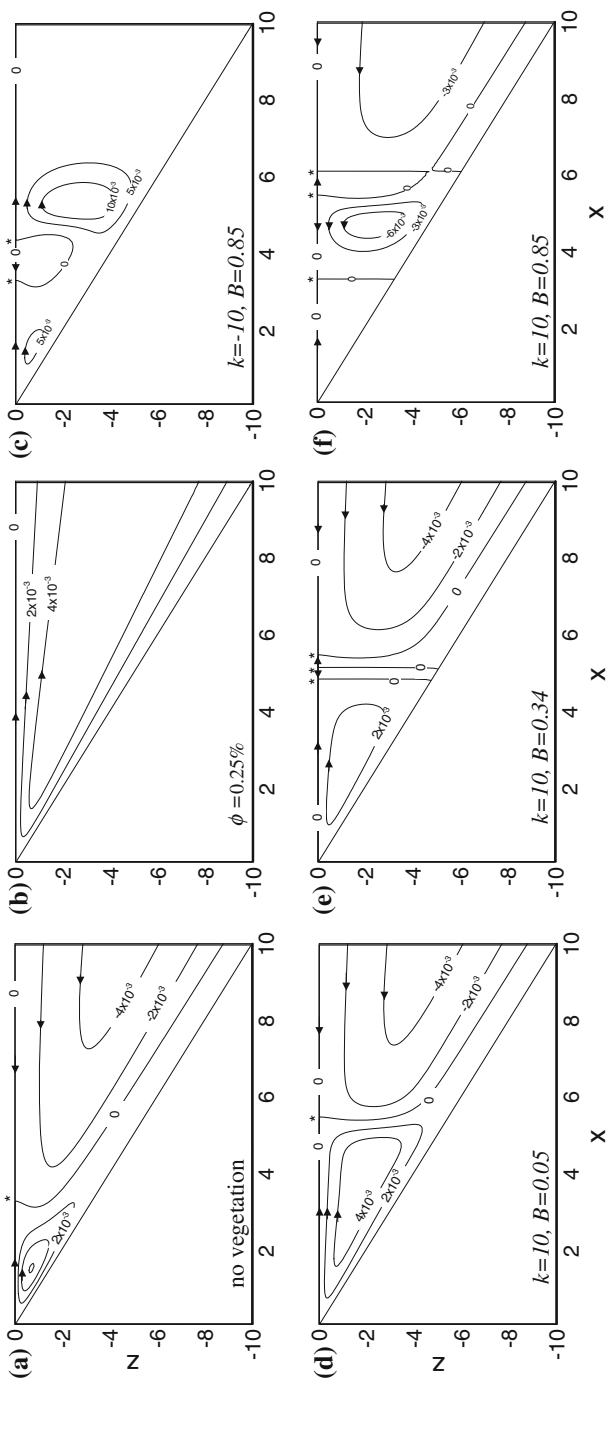

Fig. 11 Large-time streamlines at $t = 0.2$. **a** No vegetation; **b** uniform vegetation of $\phi = 0.25\,\%$ **c** open in shallow water, and vegetation in deep water; and **d–f** vegetation in shallow water, and open in deep water with different k and B values. The *asterisk* indicates the position of zero surface velocity

4.6 Verifications of horizontal velocity and exchange flow rate

By means of asymptotic solutions, horizontal velocity as well as exchange flow rates with a given bottom slope and heat flux can be estimated. As F04 indicated, ignorance of convective terms in Eq. (9) may not be suitable for typical field conditions. Instead of molecular viscosity, FP93 obtained reasonable estimates of horizontal velocity by means of eddy viscosity, which we adopt herein. Oldham and Sturman [19] measured the horizontal velocity through nighttime cooling in a wetland mesocosm (vegetation density of 17 % and diameter of 0.16 m), and obtained the maximum horizontal velocity at water surface as 2 mm/s, being in very good agreement with that of 2.2 mm/s obtained from the asymptotic solution by means of eddy viscosity ($\nu = 10^{-4}\,\mathrm{m^2\,s^{-1}}$). In addition, the stem Reynolds number $\mathrm{Re_d}$ is assumed to be small (<10 [9]), and then the linear drag law can be applied. Without any assumption, the drag coefficient can be represented as [21]:

$$C_\mathrm{D} \approx \frac{2}{\mathrm{Re_d}} \left(12 + 1.07\mathrm{Re_d}\right). \tag{36}$$

In the horizontal momentum equation, the drag term can be represented as $Cau + 1.07au\,|u|$. By means of the maximum velocity of 2.2 mm/s, vegetation density of 17 % and diameter of 0.15 m were reported by Oldham and Sturman [19], with the ratio of $Cau/\left(1.07au\,|u|\right) \approx 3.65 > 1$. Therefore, it is reasonable to neglect the second term in the right-hand side of Eq. (36).

The exchange flow rate is an indicator to evaluate the importance of thermal-driven flow on renewal of nearshore water and transport of nutrients and chemical substances between the nearshore and offshore regions. Sturman et al. [30] considered nighttime cooling as a steady-state process and linked the exchange flow rate to a bottom slope, buoyancy flux, and local water depth. Oldham and Sturman [19] extended the scaling analysis of Sturman et al. [30] and combined the principles of porous media flow to include vegetation drag. They found that the exchange flow rates are the functions of buoyancy flux, permeability of vegetated regions, and local depth, and verified with several experimental and field measurements. By means of the same parameters such as slope, water depth, incident solar radiation, and eddy viscosity ($\nu = 10^{-4}\,\mathrm{m^2\,s^{-1}}$), the derived asymptotic horizontal velocity (Eq. (20) or (21)) is adopted to estimate the exchange flow rates with and without vegetation, and verify with several previous measurements (Table 1; Fig. 12). Because some of these measurements were carried out under steady states, in order to compare with the asymptotic solutions obtained in diurnal cycles, the solar radiation from steady-state measurements was converted to the equivalent solar radiation under diurnal cycles. According to the scaling analysis in Sect. 2.2, exchange flow rates are proportional to input solar radiation, bottom slope, water depth, and inversely related with vegetation density and stem diameter. The smallest exchange flow rate was thus found at the smallest product of input solar radiation and bottom slope. The second and third datasets in Table 1 have similar input solar radiations and bottom slopes, but the presence of vegetation in the second dataset causes a smaller exchange flow rate than the third one. Overall, the asymptotic solutions show good agreements with those measurements in which water is shallower (less than 1.8 m), i.e., stratified effects can be ignored, and the assumption of uniform heat distribution over the water column is reasonable. For the field measurements conducted by Adam and Wells [10], and Monismith et al. [1], exchange flow rates were obtained at the depths of 12 and 8 m, respectively, where stratified effects are important, and the simplified assumption on heat distribution over water column may not be appropriate. In addition, the exchange flow rate with symbol of ∇ obtained from Oldham and Sturman [19] was measured with vegetation in shallow water and open in deep water

Table 1 Field and laboratory measurements

Symbol	Category	I_0 (W m^2)*	S	Depth (m)	ϕ (%)	d (m)	Data source
⋆	Lab	3	0.1	0.2	–	–	[32]
▲ a	Lab	70	0.404	0.1	17	0.0124	[19]
◇	Lab	72	0.404	0.1	–	–	[30]
▽	Field	100	0.0874	0.8	16	0.15	[19]
▲ b	Lab	300	0.404	0.1	17	0.0124	[19]
▲ c	Lab	363	0.404	0.1	17	0.0124	[19]
○	Field	200	0.0175	1.8	–	–	[30]
+	Field	250	0.02	8	–	–	[1]
×	Field	400	0.007	12	–	–	[10]

Green symbols indicate the measurements within vegetation
$^\star I_0$ is the equivalent diurnal solar radiation

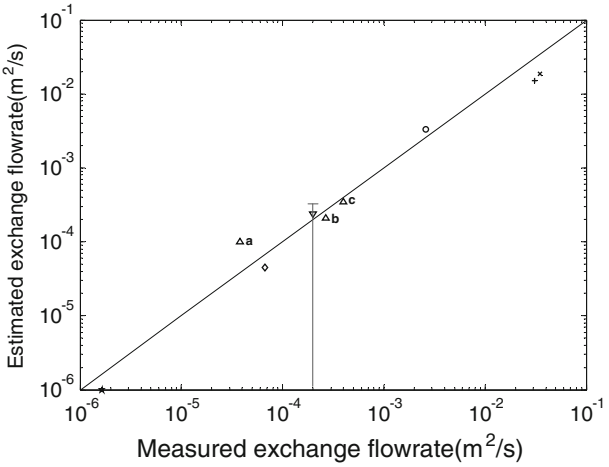

Fig. 12 Comparisons of exchange flow rates between the estimated ones from asymptotic solution and measurements. The *upwarding-triangle* and *downwarding-triangle* denote the laboratory and filed results within vegetation from [19]. The others represent the results without vegetation, which are *circle* and *diamond* from the field and the laboratory measurements by [30], *star* from the laboratory measurements by [32]. *times* and *plus* symbols from the field measurements carried out by [10] and [1]

(see Fig. 3 in Oldham and Sturman [18]). Their velocity profiles demonstrated that during nighttime, flow was from deep to shallow water along the water surface and downhill from shallow to deep water along the sloping bottom (see Fig. 4 in Oldham and Sturman [19]). As a result, blockage due to vegetation shading did not alter the flow patterns but might decrease the temperature gradient generated from topographic effects as well as exchange flow rates. Based on the results from Fig. 9a, the exchange flow rate might reduce to zero given the counterbalance of vegetation shading and topographic effects. Due to the lack of information of vegetation blockage and temperature gradient between vegetation and open water, a range of predicted exchange flow rate is provided for the case of Oldham and Sturman [19] in Fig. 12.

4.7 Limitations and valid ranges of zero-order horizontal velocity

The horizontal velocity approaches infinity in two situations:(1) at the tip of the wedge ($x \rightarrow 0$) as FP93 mentioned, and (2) when c_d is very large. At the tip, the horizontal convective terms cannot be ignored but are important only for $x < S$, which is a very small part of domain of interest (FP93). For large c_d, the dominant regions of viscous effects become smaller, and the horizontal velocity profiles experience a sharper bend near the bottom in comparison with no-vegetation case. Once c_d becomes larger, the sharp bed regime can lead to instability, which needs to be balanced by convective terms.

The asymptotic solution is valid when S^2 and $S^2\mathrm{Gr}$ are small, and stem Reynolds number $\mathrm{Re_d}$ is less than 1 to be within the linear drag law regime [21]. In order to examine the above mentioned assumptions, dimensional velocity is determined based on reasonable field parameters. The eddy viscosity used in Eq. (20) yields reasonable values for horizontal velocity, possibly because vortex sheddings generated from vegetation stems and leaves make the flow field turn turbulent. For the condition of no vegetation, horizontal velocity estimated using eddy viscosity shows good agreement with the field observation (FP93). By means of $I = 500\,\mathrm{W\,m^{-2}}$, $\nu = 10^{-4}\,\mathrm{m^2\,s^{-1}}$, stem size $d = 0.6$ cm, slope $S = 10^{-2}$, vegetation density ϕ is 0.25 %, $c_d \approx 13$, the maximum-dimensional horizontal velocity is $u' \sim 1.2 \times 10^{-2}\,\mathrm{m\,s^{-1}}$, and the corresponding $\mathrm{Re} = 0.72 < 1$, which is consistent with the assumption of linear Drag Law. In the scaling analysis, the $O\left(S^2\mathrm{Gr}\right)$ terms are omitted, which may not be suitable for typical field situation ($S = 10^{-2} \sim 10^{-3}$, $\mathrm{Gr} \approx 1.8 \times 10^7$) for ($\nu = 10^{-4}\,\mathrm{m^2\,s^{-1}}$). The valid range of the linear results can be determined by the included terms larger than the omitted terms in Eq. (9) as F04 proposed. The maximum velocity U for $\phi = 0.25$ % is $\sim 10^{-2}$. For $x \rightarrow 0$, the buoyancy is mainly balanced by the vertical shear, which yields $x < \frac{1}{S^2\mathrm{Gr}U} = \frac{100}{S^2\mathrm{Gr}}$. For $x \gg 0$, the main balance is mainly between buoyancy and vegetative drag, suggesting $x > \frac{S^2\mathrm{Gr}U}{c_d} = 7.7 \times 10^{-4} S^2\mathrm{Gr}$. Combining these two results gives $S^2\mathrm{Gr} < 360$ for the flow to be in the linear range. The valid ranges for the linear results within vegetation are wider than those without vegetation ($S^2\mathrm{Gr} < 200$ obtained in F04) as a result of reduced horizontal velocity. As the vegetation becomes denser, the smaller horizontal velocity leads to wider ranges of $S^2\mathrm{Gr}$, i.e., the convective terms in Eqs. (8) and (9) are less important. For the extreme cases, i.e., emergent vegetation in the one side, and open water in the other side, the temperature gradient generated from the vegetation shading would change the valid range of the asymptotic solutions. By considering the case of open in shallow water, and vegetation in deep water, the vegetation shading improves the topographic effect, and the range of $S^2\mathrm{Gr}$ can be obtained by comparing the unsteady and convective terms in Eq. (8), which yield $S^2\mathrm{Gr} < \left(\frac{\partial T}{\partial t}\right) / \left(u \frac{\partial T}{\partial x}\right)$. Using $B = 0.85$, $k = -10$, $x = 5$, $L_x = 10$, and the vegetation density in deep water of 0.25 %, we get the maximum horizontal velocity u of 3×10^{-2}, $\frac{\partial T}{\partial t}$ of 0.115, and $\frac{\partial T}{\partial x}$ of $1.7 \times 10^{-2}$from Eqs. (19), (33), and (35). The valid range for the linear solution is $S^2\mathrm{Gr}$ which is $S^2 Gr < 225$, narrower than that in the case with the uniform-distributed vegetation.

4.8 Second-order asymptotic solutions for temperature profiles

When the second-order temperature profile is taken into account, the tilted isotherm due to sloping bottom and advection effects can be observed (Fig. 13). The second-order temperature is related to Gr values, and larger Gr values exhibit higher nonlinearity. The Gr of 10^4 and S of 0.1 are chosen to confirm the suitability of the asymptotic solution, i.e., $S^2\mathrm{Gr} < 200$. Without vegetation, the weak stratification can be observed due to the heat advection by $u^{(0)}$ (Fig. 13a,

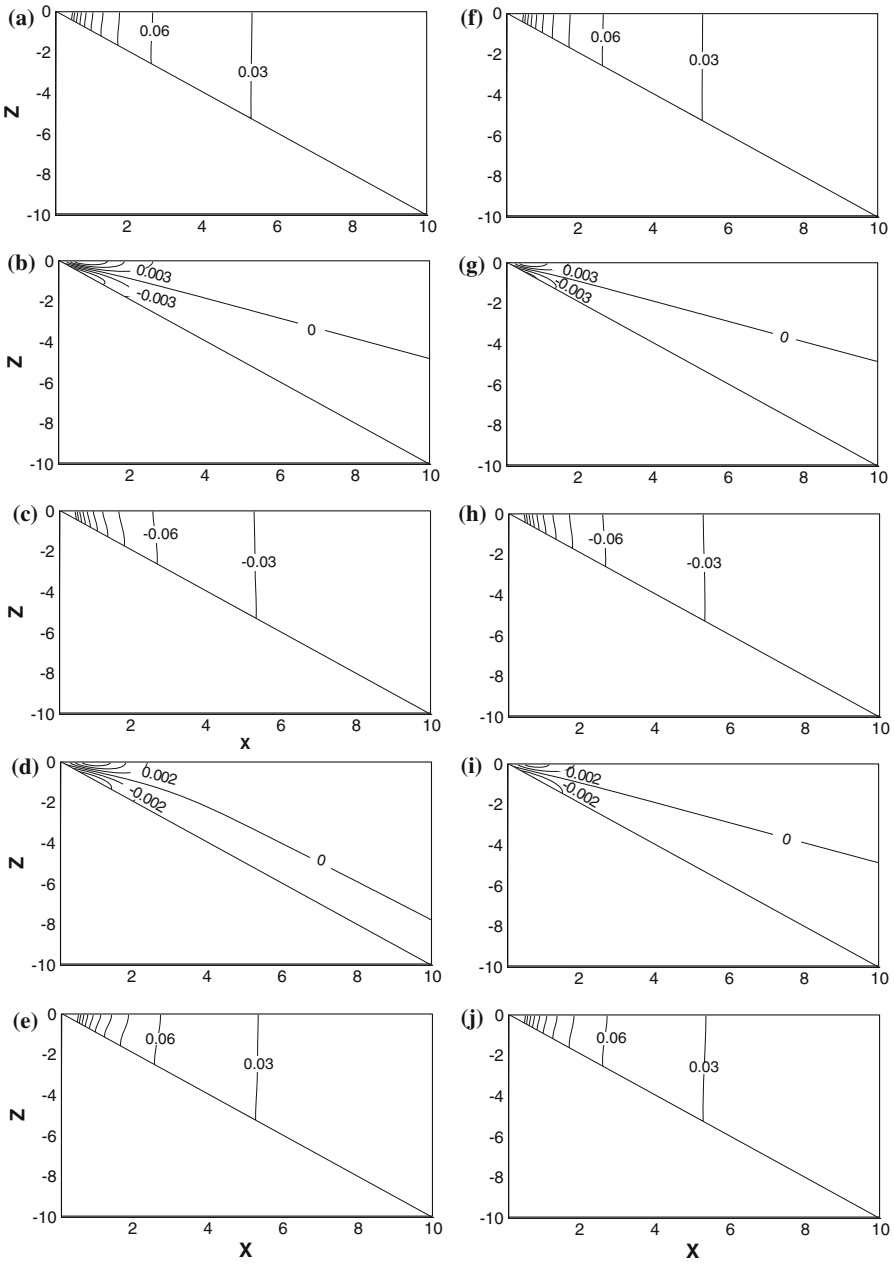

Fig. 13 Temperature isotherms (first plus second orders) for vegetation percentage of 0 % from (**a**) to (**e**) and 0.25 % from (**f**) to (**j**) at various times. The parameters of $S = 0.1$ and $\mathrm{Gr} = 10^4$ are used. (**a**) and (**f**) $t = 0.25$; (**b**) and (**g**) $t = 0.50$; (**c**) and (**h**) $t = 0.75$; (**d**) and (**i**) $t = 1$; and (**e**) and (**j**) $t = 1.25$

c, e), whereas the vegetation retards the flow and consequently keeps the temperature profiles less stratified (Fig. 13f, h, j). For $t = 0.5$, the residual heat due to velocity inertia results in higher temperature in the upper layer, and lower temperature near the bottom. The same

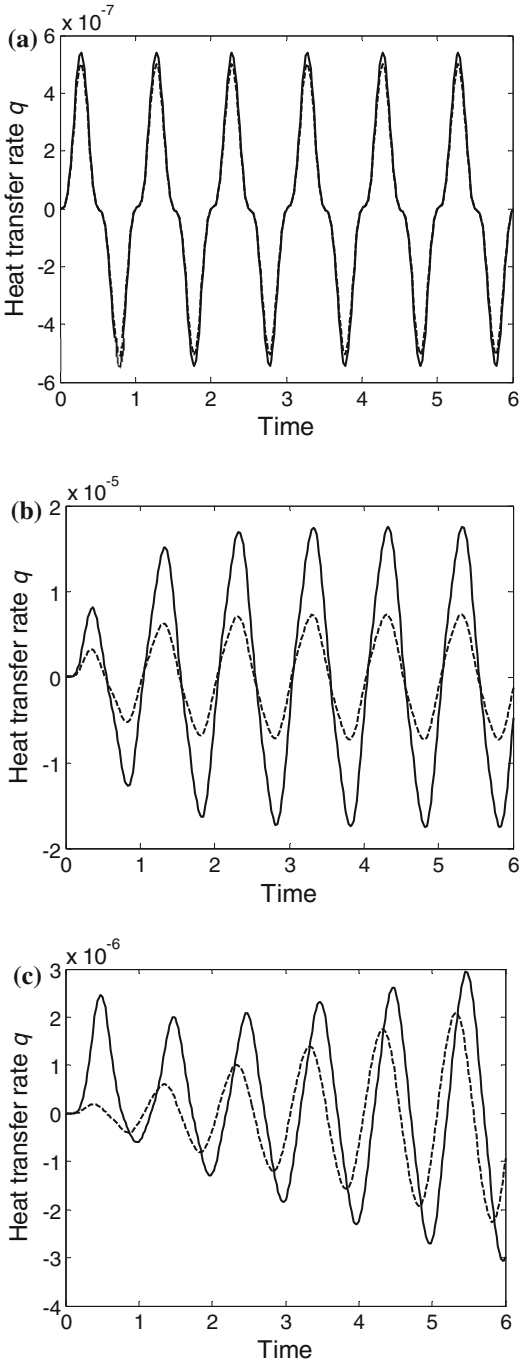

Fig. 14 Time series of horizontal heat-transfer rates q at **a** $x = 0.25$, **b** $x = 1$, and **c** $x = 5$. Heat-transfer rate q for $\phi = 0\,\%$ (*solid line*), and $\phi = 0.25\,\%$ (*dashed line*)

situations can be observed at $t = 1$. However, at $t = 1$, the zero-isotherm without vegetation is closer to the bottom, while the zero-isotherm within vegetation is approximately at the center.

The horizontal heat transfer q is proportional to the product of zero-order horizontal velocity and the second-order temperature profiles (see Sect. 3.2). Hence, q values with vegetation are smaller than q values without vegetation (Fig. 14). In shallow water ($x = 0.25$), viscosity is dominant and can diffuse into the whole water column. The effect of vegetative drag is not apparent so that q value within vegetation is slightly smaller than q values without vegetation with extremes at $t = n \pm \frac{1}{4}$. For the intermediate water depth ($x = 1$), viscosity can diffuse into the entire water depth after the first period, and consequently, the q values become purely periodic after the second cycle. For the deep water ($x = 5$), the heat-transfer rate q keeps increasing as time marches until the boundary layer grows over the entire water column (F04). Within vegetation, it takes longer time for viscosity to diffuse into the entire water column. Without vegetation, the larger inertia in deep water lags the extremity of q. The smaller inertia within vegetation leads to a smaller time lag than that without vegetation. In deep water, the extreme values of q without vegetation are observed at $t = n \pm \frac{1}{4}$, and the quarter period of forcing lag is comparable with the shallow water case. However, within 0.25 % vegetation, the time lag of q values in deep water can be reduced to the one-eighth of the forcing period.

5 Conclusions

The paper includes vegetative drag into horizontal momentum equation and discusses the thermal-driven flow field under the presence of emergent vegetation and different vegetation distributions. The horizontal velocity, exchange flow rate, and advective heat-transfer rate are significantly reduced due to the presence of vegetation. In very shallow water, the viscous effects are still dominated, but in deep water, vegetative drag counterbalances the pressure gradient and result in smaller inertia forces, i.e., smaller horizontal velocity. As a result, the phenomena of time-lag due to the inertia effects become indistinct. The flow patterns can be altered by vegetation distribution and height of emergent vegetation. Once the vegetation is tall and grows in shallow water, and if the deep water side is open, the effects of vegetation shading may interfere with the topographic effects, and the subsequent induced circulation is complicated. Variations of the vegetation blockage on the solar radiation possibly make the exchange flow rates at the centerline become zero. On the other hand, for the case of open in shallow water, and vegetation in deep water, vegetation shading can enhance the topographic effect to generate larger circulation as well as flow exchanges between the nearshore and the offshore. The two extreme cases involved with vegetation distribution can cause significant changes on exchange flowrates. Although the model ignores the light attenuation effect and vegetation distribution over vertical direction, the horizontal velocity and exchange flow rate estimated from the asymptotic solutions agree well with several field and laboratory measurements.

In order to obtain the asymptotic solution, the linear drag coefficient is applied, and the bottom slope is assumed to be small. The results of horizontal velocity indicate that the assumption of linear drag coefficient is reasonable for the thermal-driven flow. Based on the horizontal velocity estimated from the asymptotic solutions, the valid range of linear results can be up to $S^2\mathrm{Gr} < 360$ for sparse vegetation ($\phi = 0.25\,\%$). For denser vegetation, the horizontal velocity is smaller, and the range of $S^2\mathrm{Gr}$ that fits to the linear assumption can be broader. The horizontal velocity approaches infinity (1) at the tip ($x \to 0$), and (2) in dense vegetation (large drag coefficient) due to ignorance of convective terms in the governing equations.

Although the asymptotic solution can predict the magnitude of thermal-driven flow in rooted emergent vegetation for weakly stratified environment, some limitations still need to be overcome in the future. First, to make feasible analytic progresses, the model used in this study is highly idealized that the exponential decays of solar radiation during daytime and thermal instability to break residual flow and reverse the circulation during diurnal cycles are ignored. Several studies discussed the patterns of thermally driven flow in more realistic physical models [12,13,15], but researches related to vegetation effects on thermally driven flow in stratified environments are still rare [9]. The asymptotic solution is also unable to consider the penetration depth of solar radiation limited by the presence of the vegetation, which induces vertical variations of heat and should alter circulation patterns. The drag coefficient is a critical input for the analytic solution. However, the drag coefficient is usually obtained from circular cylinder tests, and the morphology (stem flexibility and leafs) of the vegetation are not included. In the asymptotic solution, the drag coefficient is assumed to be uniform along the vertical direction, and the variations of vegetative drag along the vertical direction are also neglected. In addition, the absorption or release of heat from vegetation and bottom sediments could change the flow patterns during diurnal cycles. Finally, emergent vegetation with dangling roots and submerged vegetation also grow extensively in the littoral zones, and understanding their effects on thermally driven flow is still limited to a flat bottom [18,22].

This study uses a linear model and simplified forcing mechanism to report the effect of rooted emergent vegetation on diurnal thermal-driven flow. Although the model is linear, some interesting findings are still useful for further follow-up studies. More numerical simulations and experimental investigation, however, are necessary to reveal the phenomena occurring in typical field conditions.

Appendix: Coefficients of the solution of the second-order temperature profiles

$$
\begin{aligned}
a_m(t) = {} & \frac{A}{(m\pi)^2\left(m^4\pi^2+16\sigma^2x^4\right)} \\
& \times\left[16\sigma^2x^4\left(1-\exp\left(-(m\pi/x)^2\,t/\sigma\right)\right)+m^4\pi^2\left(1-\cos(4\pi t)\right)\right. \\
& \left.-4\sigma m^2\pi x^2\sin(4\pi t)\right], \\
b_{mn}(x,t) = {} & \frac{\cos\beta_n+(\cos\beta_n-1)/\beta_n^2-\frac{1}{2}}{\left((m\pi)^2-\beta_n^2\right)\left[\left((\beta_n/x)^2+c_\mathrm{d}\right)^2+(2\pi)^2\right]\left[\beta_n^2+c_\mathrm{d}x^2\right]}, \\
c_{mn}(x,t) = {} & \left[\left(\frac{\beta_n}{x}\right)^2+c_\mathrm{d}\right]\left\{\frac{x^2\sigma\left[e^{-(m\pi/x)^2t/\sigma}-\cos(4\pi t)\right]+\frac{1}{4}m^2\pi\sin(4\pi t)}{\pi\left(m^4\pi^2+16x^4\sigma^2\right)}\right. \\
& \left.-\frac{\pi x^2\sigma\left[e^{-(m\pi/x)^2t/\sigma}-e^{-\left(\left(\frac{\beta_n}{x}\right)^2+c_\mathrm{d}\right)t}\cos(2\pi t)\right]+\frac{1}{2}\left[m^2\pi^2-\left(\beta_n^2+c_\mathrm{d}x^2\right)\sigma\right]e^{-\left[\left(\frac{\beta_n}{x}\right)^2+c_\mathrm{d}\right]t}\sin(2\pi t)}{\left[(m\pi)^2-\left(\beta_n^2+c_\mathrm{d}x^2\right)\sigma\right]^2+4\pi^2x^4\sigma^2}\right\} \\
& -\pi\frac{\frac{1}{2}m^4\pi^2\left[\cos(4\pi t)-1\right]+2\pi x^2\sigma m^2\sin(4\pi t)+8x^4\sigma^2\left[e^{-(m\pi/x)^2t/\sigma}-1\right]}{(m\pi)^2\left(m^4\pi^2+16x^4\sigma^2\right)},
\end{aligned}
\tag{37}
$$

where

$$A = \frac{1}{4\pi^2}\left(\frac{\mathrm{d}F(x)}{\mathrm{d}x}\right)^2 \left\{ \frac{\left(2 + c_\mathrm{d}x^2 - 2\cosh\left(x\sqrt{c_\mathrm{d}}\right)\right)(-1)^m x^2 \sinh\left(x\sqrt{c_\mathrm{d}}\right)}{2c_\mathrm{d}\left(m^2\pi^2 + c_\mathrm{d}x^2\right)\left(\sqrt{c_\mathrm{d}}x\cosh\left(x\sqrt{c_\mathrm{d}}\right) - \sinh\left(x\sqrt{c_\mathrm{d}}\right)\right)} \right.$$
$$- \frac{x^3\left(x\left(c_\mathrm{d}\right) - \sqrt{c_\mathrm{d}}\sinh\left(x\sqrt{c_\mathrm{d}}\right)\right)(-1)^m \sinh\left(x\sqrt{c_\mathrm{d}}\right)}{c_\mathrm{d}\left(m^2\pi^2 + c_\mathrm{d}x^2\right)\left(\sqrt{c_\mathrm{d}}x\cosh\left(x\sqrt{c_\mathrm{d}}\right) - \sinh\left(x\sqrt{c_\mathrm{d}}\right)\right)}$$
$$\left. + \frac{x^2\left(-1 + (-1)^m\right)}{c_\mathrm{d}m^2\pi^2} + \frac{x^2\left(1 - (-1)^m\cosh\left(x\sqrt{c_\mathrm{d}}\right)\right)}{c_\mathrm{d}\left[m^2\pi^2 + c_\mathrm{d}x^2\right]} \right\}. \tag{38}$$

References

1. Monismith SB, Imberger J, Morison ML (1990) Convective motion in the sidearm of a small reservoir. Limnol Oceanogr 35:1676–1702
2. James WF, Barko JW (1991) Estimation of phosphorous exchange between littoral and pelagic zones during nighttime convection circulation. Limnol Oceanogr 36(1):179–187
3. Chimney MJ, Wenkert L, Pietro KC (2006) Patterns of vertical stratification in a subtropical constructed wetland in south Florida (USA). Ecol Eng 27:322–330
4. Farrow DE, Patterson JC (1993) On the response of a reservoir sidearm to diurnal heating and cooling. J Fluid Mech 246:143–161
5. Coates MJ, Patterson JC (1993) Unsteady natural convection in a cavity with non-uniform absorption of radiation. J Fluid Mech 256:133–161
6. Lightbody A, Avener M, Nepf HM (2008) Observations of short-circuiting flow paths within a constructed treatment wetland in Augusta, Georgia, USA. Limnol Oceanogr 53(3):1040–1053
7. Lövstedt C, Bengtsson L (2008) Density-driven current between reed belts and open water in a shallow lake. Water Resour Res 44(10):W10413
8. Pokorny J, Kvet J (2004) Aquatic plants and lake ecosystem. In: O'Sullivan PE, Reynolds CS (eds) The lakes handbook, vol 1. Blackwell, Oxford, pp 309–340
9. Zhang X, Nepf HM (2009) Thermally driven exchange flow between open water and an aquatic canopy. J Fluid Mech 632:227–243
10. Adams EE, Wells SA (1984) Field measurements on side arms of Lake Anna, VA. J Hydraul Eng ASCE 110:773–793
11. Farrow DE (2004) Periodically forced natural convection over slowly varying topography. J Fluid Mech 508:1–21
12. Farrow DE, Patterson JC (1994) The daytime circulation and temperature pattern in a reservoir sidearm. Int J Heat Mass Transf 37:1957–1968
13. Lei C, Patterson JC (2002) Unsteady natural convection in a triangular enclosure induced by absorption of radiation. J Fluid Mech 460:181–209
14. Mao Y, Lei C, Patterson JC (2009) Unsteady natural convection in a triangular enclosure induced by absorption of radiation—a revisit by improved scaling analysis. J Fluid Mech 622:75–102
15. Lei C, Patterson JC (2006) Natural convection induced by diurnal heating and cooling in a reservoir with slowly varying topography. JSME Int J B 49:605–615
16. Mao Y, Lei C, Patterson JC (2010) Unsteady near-shore natural convection induced by surface cooling. J Fluid Mech 642:213–233
17. Farrow DE (2013) Periodically driven circulation near the shore of a lake. Environ Fluid Mech 13(3):243–255
18. Coates M, Ferris J (1994) The radiatively-driven natural convection beneath a floating plant layer. Limnol Oceanogr 39(5):1186–1194
19. Oldham CE, Sturman JJ (2001) The effect of emergent vegetation on convective flushing in shallow wetlands: scaling and experiment. Limnol Oceanogr 46(6):1486–1493
20. Zhang X, Nepf HM (2008) Density driven exchange flow between open water and an aquatic canopy. Water Resour Res 44(8):W08417
21. Tanino Y, Nepf HM, Kulis PS (2005) Gravity current in aquatic canopies. Water Resour Res 41(12):W12402
22. Zhang X, Nepf HM (2011) Exchange flow between open water and floating vegetation. Environ Fluid Mech 11(5):531–546

23. Koch DL, Ladd AJC (1997) Moderate Reynolds number flows through periodic and random arrays of aligned cylinders. J Fluid Mech 349:31–66
24. Jamali M, Zhang X, Nepf HM (2008) Exchange flow between a canopy and open water. J Fluid Mech 611:237–254
25. Cormack DE, Leal LG, Imberger J (1974) Natural convection in a shallow cavity with differentially heated end walls. Part 1. Asymptotic theory. J Fluid Mech 65:209–229
26. Poulikakos D, Bejan A (1983) The fluid dynamics of an attic space. J Fluid Mech 131:251–269
27. Brown J, Churchill R (2009) Complex variables and applications. McGraw-Hill, New York
28. Farrow DE (1991) Unsteady natural convection in reservoir sidearms. Dissertation, University of Western Australia
29. Horsh GM, Stefan HG (1988) Convective circulation in littoral water due to surface cooling. Limnol Oceanogr 33(5):1068–1083
30. Sturman JJ, Oldham CE, Ivey GN (1999) Steady convective exchange flows down slopes. Aquat Sci 61:260–278
31. Chubarenko IP (2010) Horizontal convective water exchange above a sloping bottom: the mechanism of its formation and an analysis of its development. Oceanology 50(2):166–174
32. Chubarenko IP, Demchenko NY (2008) Laboratory modeling of the structure of a thermal bar and related circulation in a basin with a sloping bottom. Oceanology 48(3):356–370